

# **ELECTRON INTERACTIONS IN CARBON NANOMATERIALS**

by

Brian Andrew Barth

B.S. Chemistry, University of Pittsburgh, 2009

Submitted to the Graduate Faculty of

The Kenneth P. Dietrich School of Arts and Sciences in partial fulfillment

of the requirements for the degree of

Master of Science

University of Pittsburgh

2012

UNIVERSITY OF PITTSBURGH  
KENNETH P. DIETRICH SCHOOL OF ARTS AND SCIENCES

This thesis was presented

by

Brian Andrew Barth

It was defended on

April 11, 2012

and approved by

Dr. Geoffrey Hutchison, Assistant Professor, Chemistry

Dr. Renã A. S. Robinson, Assistant Professor, Chemistry

Thesis Director: Dr. Alexander Star, Associate Professor, Chemistry

Copyright © by Brian Barth

2012

# **ELECTRON INTERACTIONS IN CARBON NANOTUBES**

Brian Barth, M.S.

University of Pittsburgh, 2012

The following research reflects two areas of interest in carbon nanomaterials: (1) enzymatic oxidation and (2) photocatalytic applications.

Horseradish peroxidase (HRP) is known to catalyze oxidation of carbon nanomaterials. Here, we closely examine the kinetics of enzymatic oxidation of carbon nanotubes (CNTs) using HRP. We show that CNTs oxidized by harsh acid treatment become shorter, more defective, and lose their specific absorption bands and fluorescent signals. After treatment with HRP and  $H_2O_2$ , these oxidized CNTs show a decrease in average CNT length, a decrease in defective area, and return of characteristic absorption bands and fluorescence. We observed that CNTs chemically oxidized using weaker oxidation treatment were shortened, slightly more defective than before acid treatment, did not lose their characteristic absorption bands, but did lose fluorescence. After treatment with HRP and  $H_2O_2$  there was a decrease in length, a decrease in defective area, no observed change in absorption spectra bands and fluorescent signal did not return.  $H_2O_2$  treated oxidized CNTs, showed similar results to HRP treated samples but did not recover their fluorescent signals.

$TiO_2$  is a popular photocatalyst due to its small band gap, low cost, and low toxicity. Limitations in photocatalysis using  $TiO_2$  are due to electron – hole recombination following electron excitation from the valence band to conduction band. Efforts to retard electron – hole recombination involve doping  $TiO_2$  with metals, which have electron trapping sites on their surfaces. Carbon nanomaterials show promise as  $TiO_2$  dopants due to their large surface area,

electron storage capacity, and interaction with metal oxide surface groups. Here, we demonstrate synthesis of TiO<sub>2</sub> – carbon nanomaterials using sol – gel techniques and that electron transfer is possible under UV irradiation. Comparing synthesized TiO<sub>2</sub>-SWNTs and commercially available anatase TiO<sub>2</sub> nanoparticles, we find no significant improvement in photocatalytic oxidation of dye. Furthermore, TiO<sub>2</sub> – SWNTs do not photoreduce CO<sub>2</sub>. P25 TiO<sub>2</sub> nanoparticles oxidize dye in these studies, and have demonstrated the ability to reduce CO<sub>2</sub> in published works. Lack of homogeneity in the TiO<sub>2</sub> crystalline structure may be responsible for these differences. We show prolonged UV exposure may degrade TiO<sub>2</sub> – carbon photocatalysts, possibly through ROS generation.

## TABLE OF CONTENTS

<b>1.0</b>	<b>INTRODUCTION.....</b>	<b>1</b>
<b>1.1</b>	<b>STRUCTURE OF CARBON NANOMATERIALS.....</b>	<b>1</b>
<b>1.2</b>	<b>CHARACTERIZATION OF SWNTS.....</b>	<b>6</b>
<b>1.2.1</b>	<b>TEM .....</b>	<b>6</b>
<b>1.2.2</b>	<b>Spectroscopy .....</b>	<b>8</b>
<b>1.2.3</b>	<b>Enzymatic Oxidation of SWNTs.....</b>	<b>10</b>
<b>1.2.4</b>	<b>TiO<sub>2</sub> – Carbon Nanomaterial Photocatalysis .....</b>	<b>14</b>
<b>2.0</b>	<b>MECHANISTIC STUDY OF THE ENZYMATIC OXIDATION OF CARBON NANOTUBES.....</b>	<b>16</b>
<b>2.1</b>	<b>EXPERIMENTAL DETAILS .....</b>	<b>17</b>
<b>2.1.1</b>	<b>Chemical Oxidation and Characterization of SWNTs.....</b>	<b>17</b>
<b>2.1.2</b>	<b>Enzymatic Oxidation of SWNTs Using Horseradish Peroxidase .....</b>	<b>20</b>
<b>2.2</b>	<b>RESULTS AND DISCUSSION .....</b>	<b>21</b>
<b>2.2.1</b>	<b>Characterization of Chemically Oxidized SWNTs .....</b>	<b>21</b>
<b>2.2.2</b>	<b>Enzymatic Oxidation of Chemically Oxidized SWNTs.....</b>	<b>26</b>
<b>2.3</b>	<b>CONCLUSIONS .....</b>	<b>32</b>
<b>3.0</b>	<b>TiO<sub>2</sub> – CARBON NANOMATERIALS PHOTOCATALYSTS .....</b>	<b>34</b>
<b>3.1</b>	<b>EXPERIMENTAL DETAILS .....</b>	<b>35</b>

3.1.1	Synthesis and Characterization .....	35
3.1.2	Dye Degradation.....	35
3.1.3	CO <sub>2</sub> Reduction.....	36
3.2	RESULTS .....	37
3.2.1	Synthesis and Characterization .....	37
3.2.2	Dye Degradation.....	41
3.2.3	CO <sub>2</sub> reduction.....	47
APPENDIX A .....		50
APPENDIX B .....		65
BIBLIOGRAPHY .....		69

## LIST OF FIGURES

Figure 1 Physical structure of carbon nanotubes .....	3
Figure 2 Electronic structure of carbon nanotubes .....	5
Figure 3 Raman Spectrum of HiPco SWNTs .....	9
Figure 4 Horseradish Peroxidase (HRP) (a) structure of HRP adapted from reference 23 (b) peroxidase cycle oxidation involving HRP adapted from reference 26 .....	12
Figure 5 HRP binding site depicting amino acid residues surrounding hemin catalytic center adapted from reference 23 .....	13
Figure 6 TiO <sub>2</sub> photocatalysis (a) photocatalytic oxidation and reduction on pure TiO <sub>2</sub> and (b) metal doped TiO <sub>2</sub> .....	15
Figure 7 Characterization of H <sub>2</sub> SO <sub>4</sub> / HNO <sub>3</sub> oxidized HiPco SWNTs (batch 1) (a) TEM image (b) Raman spectrum (c) UV-VIS-NIR spectrum .....	22
Figure 8 Characterization of H <sub>2</sub> SO <sub>4</sub> / HNO <sub>3</sub> oxidized HiPco SWNTs (batch 2) (a) TEM image (b) Raman spectrum (c) UV-VIS-NIR spectrum (d) FTIR spectrum .....	23
Figure 9 Characterization of H <sub>2</sub> SO <sub>4</sub> / H <sub>2</sub> O <sub>2</sub> oxidized HiPco SWNTs (a) TEM image (b) Raman spectrum (c) UV-VIS-NIR spectrum (d) FTIR spectrum .....	25
Figure 10 Fenton catalysis .....	26

Figure 11 Characterization of HRP treated  $H_2SO_4 / HNO_3$  oxidized HiPco SWNTs (a) Length vs. time plot determined from TEM images (b) Normalized D/G ratio vs. time determined from Raman spectra (c) UV-VIS- NIR spectra for batch 1 samples treated with HRP and  $H_2O_2$  (d) UV-VIS-NIR spectra for batch 2 samples treated with  $H_2O_2$  (-HRP) ..... 29

Figure 12 PL mapping data for HRP treated  $H_2SO_4 / HNO_3$  oxidized HiPco SWNTs (a) pristine HiPco SWNTs prior to oxidative treatment (b) HiPco SWNT oxidized with sulfuric/nitric acid mixture (c) HRP (d) HiPco SWNT oxidized with sulfuric/nitric acid mixture after 35 days of  $H_2O_2$  additions while incubated with 1.54 mg HRP (e) HiPco SWNT oxidized with sulfuric/nitric acid mixture after 35 days of  $H_2O_2$  additions while incubated with 0.1 mg HRP (f) HiPco SWNT oxidized with sulfuric/nitric acid mixture after 49 days of  $H_2O_2$  ( - HRP) ..... 30

Figure 13 Characterization of HRP treated  $H_2SO_4 / H_2O_2$  oxidized HiPco SWNTs (a) Length vs. time determined from TEM images (b) Normalized D/G ratio vs. time determined from Raman spectra (c) UV-VIS-NIR spectra comparing oxidized SWNTs, oxidized SWNTs treated with HRP and  $H_2O_2$  for 42 days, and oxidized SWNTs treated with  $H_2O_2$  for 42 days..... 31

Figure 14 PL mapping data for HRP treated  $H_2SO_4 / H_2O_2$  oxidized HiPco SWNTs (a) HiPco SWNTs oxidized with  $H_2SO_4 / H_2O_2$  (b) After 42 days of  $H_2O_2$  additions while incubated with 1.54 mg HRP (c) After 42 days of  $H_2O_2$  additions while incubated with 0.1 mg HRP (d) After 42 days of  $H_2O_2$  additions ( - HRP )..... 32

Figure 15  $CO_2$  reduction experimental design..... 37

Figure 16 Ether elimination ..... 38

Figure 17 TEM images of  $TiO_2$  – carbon nanomaterials (a)  $TiO_2$  – SWNTs (b)  $TiO_2$  – GO..... 39

Figure 18 TiO <sub>2</sub> – surface functional group interactions five possible interactions between TiO <sub>2</sub> and surface functional groups (Ti atom is represented in these diagrams as M) adapted from reference 50.....	40
Figure 19 TiO <sub>2</sub> Raman spectra (a) Raman spectra of TiO <sub>2</sub> photocatalysts and SWNTs (b) zoomed in view of (a) (c) Raman spectra of anatase and amorphous TiO <sub>2</sub> adapted from reference 51.....	40
Figure 20 Structure of methyl orange .....	41
Figure 21 Dye degradation with different photocatalysts.....	44
Figure 22 Photocatalytic electron transfer in TiO <sub>2</sub> – GO (a) Illustration of electron transfer in TiO <sub>2</sub> – GO heterogeneous photocatalysts (b) TiO <sub>2</sub> – GO before and after UV irradiation .....	45
Figure 23 TiO <sub>2</sub> – GO before and after UV exposure (a) before UV (b) after 30 hours of UV exposure with 100W, 365nm lamp .....	46
Figure 24 CO <sub>2</sub> reduction mechanisms adapted from reference 30 .....	48
Figure 25 CO <sub>2</sub> reduction MS data (a) MS reduction data (b) close up view of m/z values 8 – 33 from spectra shown in (a) .....	49
Figure 26 HRP (1.54 mg) + H <sub>2</sub> O <sub>2</sub> treated H <sub>2</sub> SO <sub>4</sub> / HNO <sub>3</sub> oxidized HiPco SWNTs day 14.....	50
Figure 27 (1.54 mg) + H <sub>2</sub> O <sub>2</sub> treated H <sub>2</sub> SO <sub>4</sub> / HNO <sub>3</sub> oxidized HiPco SWNTs day 28.....	51
Figure 28 HRP (0.1 mg) + H <sub>2</sub> O <sub>2</sub> treated H <sub>2</sub> SO <sub>4</sub> / HNO <sub>3</sub> oxidized HiPco SWNTs day 14.....	51
Figure 29 HRP (0.1 mg) + H <sub>2</sub> O <sub>2</sub> treated H <sub>2</sub> SO <sub>4</sub> / HNO <sub>3</sub> oxidized HiPco SWNTs day 28.....	52
Figure 30 HRP (0.1 mg) + H <sub>2</sub> O <sub>2</sub> treated H <sub>2</sub> SO <sub>4</sub> / HNO <sub>3</sub> oxidized HiPco SWNTs day 35.....	52
Figure 31 H <sub>2</sub> O <sub>2</sub> treated (- HRP) H <sub>2</sub> SO <sub>4</sub> / HNO <sub>3</sub> oxidized HiPco SWNTs day 14.....	53
Figure 32 H <sub>2</sub> O <sub>2</sub> treated (- HRP) H <sub>2</sub> SO <sub>4</sub> / HNO <sub>3</sub> oxidized HiPco SWNTs day 21 .....	53
Figure 33 H <sub>2</sub> O <sub>2</sub> treated (- HRP) H <sub>2</sub> SO <sub>4</sub> / HNO <sub>3</sub> oxidized HiPco SWNTs day 28.....	54
Figure 34 H <sub>2</sub> O <sub>2</sub> treated (- HRP) H <sub>2</sub> SO <sub>4</sub> / HNO <sub>3</sub> oxidized HiPco SWNTs day 35.....	54

Figure 35 H <sub>2</sub> O <sub>2</sub> treated (- HRP) H <sub>2</sub> SO <sub>4</sub> / HNO <sub>3</sub> oxidized HiPco SWNTs day 42.....	55
Figure 36 H <sub>2</sub> O <sub>2</sub> treated (- HRP) H <sub>2</sub> SO <sub>4</sub> / HNO <sub>3</sub> oxidized HiPco SWNTs day 49 .....	55
Figure 37 HRP (1.54 mg) + H <sub>2</sub> O <sub>2</sub> treated H <sub>2</sub> SO <sub>4</sub> / H <sub>2</sub> O <sub>2</sub> oxidized HiPco SWNTs day 7 .....	56
Figure 38 HRP (1.54 mg) + H <sub>2</sub> O <sub>2</sub> treated H <sub>2</sub> SO <sub>4</sub> / H <sub>2</sub> O <sub>2</sub> oxidized HiPco SWNTs day 14 .....	56
Figure 39 HRP (1.54 mg) + H <sub>2</sub> O <sub>2</sub> treated H <sub>2</sub> SO <sub>4</sub> / H <sub>2</sub> O <sub>2</sub> oxidized HiPco SWNTs day 21 .....	57
Figure 40 HRP (1.54 mg) + H <sub>2</sub> O <sub>2</sub> treated H <sub>2</sub> SO <sub>4</sub> / H <sub>2</sub> O <sub>2</sub> oxidized HiPco SWNTs day 28 .....	57
Figure 41 HRP (1.54 mg) + H <sub>2</sub> O <sub>2</sub> treated H <sub>2</sub> SO <sub>4</sub> / H <sub>2</sub> O <sub>2</sub> oxidized HiPco SWNTs day 35 .....	58
Figure 42 HRP (1.54 mg) + H <sub>2</sub> O <sub>2</sub> treated H <sub>2</sub> SO <sub>4</sub> / H <sub>2</sub> O <sub>2</sub> oxidized HiPco SWNTs day 42 .....	58
Figure 43 HRP (0.1 mg) + H <sub>2</sub> O <sub>2</sub> treated H <sub>2</sub> SO <sub>4</sub> / H <sub>2</sub> O <sub>2</sub> oxidized HiPco SWNTs day 7 .....	59
Figure 44 HRP (0.1 mg) + H <sub>2</sub> O <sub>2</sub> treated H <sub>2</sub> SO <sub>4</sub> / H <sub>2</sub> O <sub>2</sub> oxidized HiPco SWNTs day 14 .....	59
Figure 45 HRP (0.1 mg) + H <sub>2</sub> O <sub>2</sub> treated H <sub>2</sub> SO <sub>4</sub> / H <sub>2</sub> O <sub>2</sub> oxidized HiPco SWNTs day 21 .....	60
Figure 46 HRP (0.1 mg) + H <sub>2</sub> O <sub>2</sub> treated H <sub>2</sub> SO <sub>4</sub> / H <sub>2</sub> O <sub>2</sub> oxidized HiPco SWNTs day 28 .....	60
Figure 47 HRP (0.1 mg) + H <sub>2</sub> O <sub>2</sub> treated H <sub>2</sub> SO <sub>4</sub> / H <sub>2</sub> O <sub>2</sub> oxidized HiPco SWNTs day 35 .....	61
Figure 48 HRP (0.1 mg) + H <sub>2</sub> O <sub>2</sub> treated H <sub>2</sub> SO <sub>4</sub> / H <sub>2</sub> O <sub>2</sub> oxidized HiPco SWNTs day 42 .....	61
Figure 49 H <sub>2</sub> O <sub>2</sub> treated (- HRP) H <sub>2</sub> SO <sub>4</sub> / H <sub>2</sub> O <sub>2</sub> oxidized HiPco SWNTs day 7.....	62
Figure 50 H <sub>2</sub> O <sub>2</sub> treated (- HRP) H <sub>2</sub> SO <sub>4</sub> / H <sub>2</sub> O <sub>2</sub> oxidized HiPco SWNTs day 14 .....	62
Figure 51 H <sub>2</sub> O <sub>2</sub> treated (- HRP) H <sub>2</sub> SO <sub>4</sub> / H <sub>2</sub> O <sub>2</sub> oxidized HiPco SWNTs day 21 .....	63
Figure 52 H <sub>2</sub> O <sub>2</sub> treated (- HRP) H <sub>2</sub> SO <sub>4</sub> / H <sub>2</sub> O <sub>2</sub> oxidized HiPco SWNTs day 28 .....	63
Figure 53 H <sub>2</sub> O <sub>2</sub> treated (- HRP) H <sub>2</sub> SO <sub>4</sub> / H <sub>2</sub> O <sub>2</sub> oxidized HiPco SWNTs day 35 .....	64
Figure 54 H <sub>2</sub> O <sub>2</sub> treated (- HRP) H <sub>2</sub> SO <sub>4</sub> / H <sub>2</sub> O <sub>2</sub> oxidized HiPco SWNTs day 42 .....	64
Figure 55 HRP (1.54 mg) + H <sub>2</sub> O <sub>2</sub> treated H <sub>2</sub> SO <sub>4</sub> / HNO <sub>3</sub> oxidized HiPco SWNTs .....	65
Figure 56 HRP (0.1 mg) + H <sub>2</sub> O <sub>2</sub> treated H <sub>2</sub> SO <sub>4</sub> / HNO <sub>3</sub> oxidized HiPco SWNTs .....	66
Figure 57 H <sub>2</sub> O <sub>2</sub> treated (- HRP) H <sub>2</sub> SO <sub>4</sub> / HNO <sub>3</sub> oxidized HiPco SWNTs.....	66

Figure 58 HRP (1.54 mg) + H <sub>2</sub> O <sub>2</sub> treated H <sub>2</sub> SO <sub>4</sub> / H <sub>2</sub> O <sub>2</sub> oxidized HiPco SWNTs .....	67
Figure 59 HRP (0.1 mg) + H <sub>2</sub> O <sub>2</sub> treated H <sub>2</sub> SO <sub>4</sub> / H <sub>2</sub> O <sub>2</sub> oxidized HiPco SWNTs .....	67
Figure 60 H <sub>2</sub> O <sub>2</sub> treated (- HRP) H <sub>2</sub> SO <sub>4</sub> / H <sub>2</sub> O <sub>2</sub> oxidized HiPco SWNTs .....	68

## LIST OF EQUATIONS

Equation 1 Roll up vector .....	2
Equation 2 Electronic properties of carbon nanotubes .....	3
Equation 3 Microscope resolution approximation .....	7
Equation 4 Effective electron wavelength, defined by de Broglie relationship .....	7

## **1.0 INTRODUCTION**

Nanotechnology, the study of manipulating materials with dimensions on the order of 1 to 100 nm, is a novel and rapidly growing scientific field. Since the year 2000, when the US National Nanotechnology Initiative was introduced, world funding for nanotechnology research has grown from \$1 billion to \$10 billion and is anticipated to increase another 20% over the next three years.<sup>1</sup> Applications of nanotechnology, especially the use of carbon based nanomaterials, have shown the potential to revolutionize manufacturing, electronics, and biomedical industries.<sup>2-5</sup> Carbon based nanomaterials include: fullerenes, carbon nanotubes (CNTs), graphene, and nanodiamonds (NDs), among which carbon nanotubes and graphene have received the most attention to date.

### **1.1 STRUCTURE OF CARBON NANOMATERIALS**

Interest in carbon nanomaterials has grown due to their physical, chemical, and electronic properties. Graphene, one allotrope of carbon, is a sheet of  $sp^2$  hybridized carbon of single atom thickness. CNTs are hollow cylinders of  $sp^2$  hybridized carbon, and exist in single-walled and multi-walled varieties. A single-walled carbon nanotube (SWNT) can be qualitatively described as a layer of graphene, rolled up, as shown in Figure 1 (a).<sup>6</sup> Multi-walled nanotubes (MWNTs)

are structures comprised of concentric SWNTs, as shown in Figure 1 (c).<sup>7</sup> Reports of synthesized CNTs have existed since the 1950's, but their discovery is usually credited to Sumio Iijima who synthesized them during an arc discharge procedure in 1991.<sup>8</sup> Desire to use nanotubes or graphene in processing, requires oxidation of the hydrophobic sp<sup>2</sup> lattice in order to make these carbon nanomaterials water soluble. An example of the structure of graphene oxide (GO), a graphene sheet with oxygen functionalities (-C=O, -COOH, -COC-, -OH) generated from acid treatment, is shown in Figure 1 (d).<sup>9</sup>

If CNTs are thought about as a rolled up sheet of graphene, the chirality, the orientation in which the sheet is rolled, affects the electronic and optical properties of the nanotube.<sup>10-13</sup> Figure 1(b)<sup>14</sup> illustrates possible roll up vectors for generating SWNTs of varying chirality. Any two lattice points on a graphene sheet can be connected, along a circumferential roll up vector, to generate a SWNT. The roll up vector labeled C<sub>h</sub>, shown in Equation 1, is equal to the linear combination of the unit vectors, a<sub>1</sub> and a<sub>2</sub>, with indices given as (n, m).

$$C_h = na_1 + ma_2 = (n,m)$$

**Equation 1 Roll up vector**

SWNTs with indices (n, 0) and (n, n) have unique symmetries and are labeled as zigzag and armchair nanotubes, respectively. SWNTs with indices (n, m) are labeled as chiral. Mathematical approximations for electronic properties of SWNTs in relation to their symmetries are given in Equations 2 (a, b).<sup>6</sup>

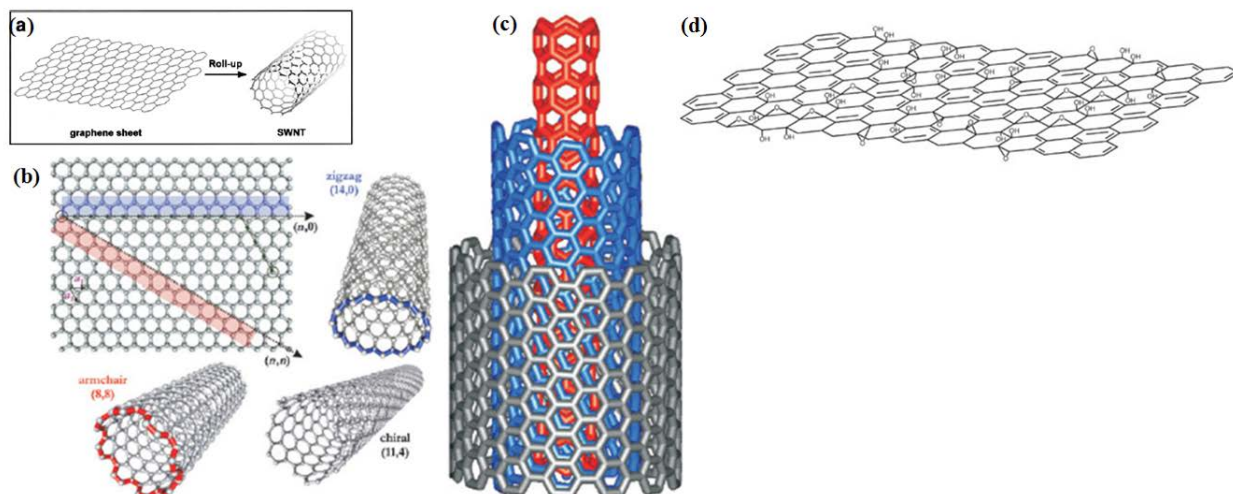


**Figure 1 Physical structure of carbon nanotubes** a) qualitative description of SWNT as “rolled up” graphene sheet adapted from reference 6 (b) chirality of SWNT based on “roll up” vector adapted from reference 7 (c) drawing of MWNT adapted from reference 7 (d) functional groups on graphene oxide adapted from reference 9

Metallic NTs  $(n - m) / 3 = k$ , where k is an integer (a)

Semiconducting NTs  $(n - m) / 3 \neq k$ , where k is an integer (b)

**Equation 2 Electronic properties of carbon nanotubes**

SWNTs with indices  $(n - m) / 3 = k$ , where k is an integer, are classified as metallic;  $(n - m) / 3 \neq k$  are classified as semiconducting. The distinction between metallic and semiconducting CNTs is made based on their energy band structures, the allowed and forbidden occupation of energy levels by electrons. In small molecules, atomic orbitals (AO's) of neighboring atoms can combine to form bonding and antibonding molecular orbitals (MO's), with energy levels lower and higher, respectively, to those of the original AO's. In solids comprised of many atoms, bonding and antibonding MO's from each bond between atoms are at slightly different energies. Due to the large number of bonds at slightly different energy levels, the bonding and antibonding

MO's are approximated as continuous bands. The valence and conduction bands, of the solid material, can be thought of qualitatively as highest occupied (HOMO) and lowest unoccupied molecular orbitals (LUMO), respectively.<sup>15</sup> Semiconductors have electronic band structures with gaps of forbidden energy levels between the valence and conduction bands, while metals have a continuous band structure of allowed energy levels without a gap. A band diagram for SWNTs with semiconducting and metallic band structure is shown in Figure 2 (a). Energy of bands is plotted versus density of states (DOS), the number of states allowed for electron occupation at a particular energy. The spike shape of the bands, known as van Hove singularities, is generated by the quasi one-dimensional structure of SWNTs, which force quantum confinement on the  $\pi$  electrons in the system.<sup>6</sup> Electronic transitions between symmetric van Hove singularities can be induced by absorption of photons using ultraviolet-visible-near infrared (UV-VIS-NIR) light, as used in absorption spectroscopy. These electronic transitions give peaks in the absorption spectrum at wavelengths corresponding to the transition energy and are labeled as  $M_{11}$ ,  $S_{11}$ , and  $S_{22}$ , for a metallic and two semiconducting transitions,<sup>16</sup> respectively, as shown in Figure 2.

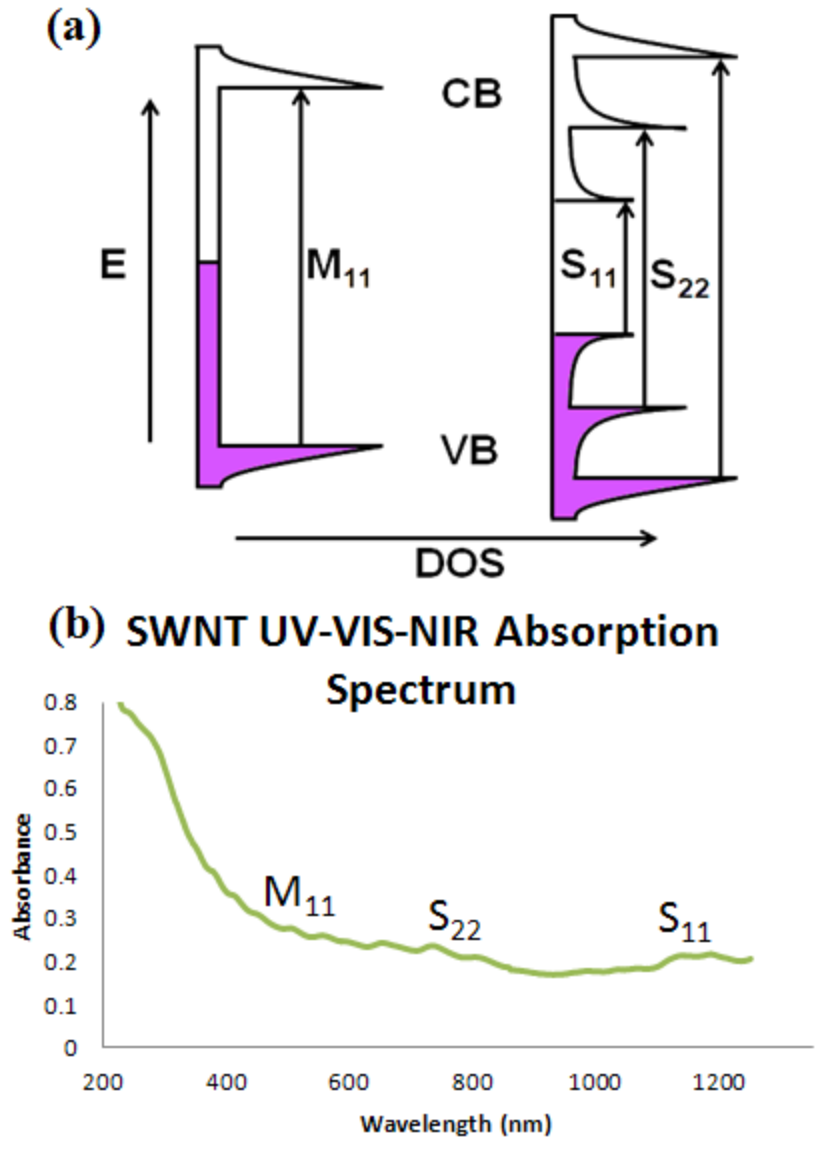


**Figure 2 Electronic structure of carbon nanotubes** (a) DOS diagram of semiconducting and metallic SWNTs (b) UV-VIS-NIR absorption spectrum of HiPco SWNTs

Nanotubes of different diameters will have slightly different transition energies, which creates an absorption spectrum with many overlapping peaks and can generate broad bands. Semiconducting SWNTs have small band gaps of approximately 1.1eV<sup>17</sup>, and while metallic SWNT do not have a band gap, they have a transition because of the curvature of the sp<sup>2</sup> lattice. The electronic properties of SWNTs, as well as large surface areas, and electron storage capacity of 1 electron for every 32 carbon atoms<sup>18</sup>, make them ideal candidates for incorporation in electronic devices and photocatalysts.

## **1.2 CHARACTERIZATION OF SWNTS**

Due to the heterogeneous nature of CNT samples, a variety of characterization techniques are utilized, such as transmission electron microscopy (TEM), ultraviolet-visible-near infrared (UV-VIS-NIR) absorption spectroscopy, Fourier transform infrared (FTIR) spectroscopy and Raman spectroscopy. Here, the mentioned techniques will be described in more detail.

### **1.2.1 TEM**

CNTs have diameters on the order of nanometers. Optical microscopy is unable to resolve features this small because of the wavelength of visible light, as shown in Equation 3. Therefore, electron microscopy must be implemented to observe nanometer size materials. Resolution can be approximated as:

$$d = \frac{\lambda}{2NA}$$

**Equation 3 Microscope resolution approximation**

where  $d$  is maximum resolution,  $\lambda$  is the wavelength of light, and  $NA$  is the numerical aperture of the system. There is little change in the value of  $NA$ , therefore wavelength is the limiting factor for improving maximum resolution. Visible light has a wavelength range of approximately 400 – 700 nm, however the effective wavelength of an electron accelerated from an electron source using a 100KeV potential, a standard value for TEM, has a wavelength of 0.0037nm, according to Equation 4,

$$\lambda = \frac{h}{\sqrt{2m_0E(1 + \frac{E}{2m_0c^2})}}$$

**Equation 4 Effective electron wavelength, defined by de Broglie relationship**

where  $h$  is Planck's constant,  $m_0$  is the rest mass of an electron,  $E$  is the energy of the accelerated electron, and  $c$  is the speed of light. While resolution using a 100keV electron gun is hypothetically calculated to be 0.0037nm, in reality, it is limited by imperfections in the electron lenses. The electron source is an electron gun that uses a tungsten filament, which when a high current is passed through it, emits electrons. The electron path is manipulated by electromagnetic lenses and focused on a stage containing a specimen, which interacts with the electron beam. Some electrons are scattered as they hit the sample, while others pass through and hit a fluorescent screen, which is viewed. TEM can be used for imaging SWNTs but does not give information about their structure; this information must be gained through spectroscopy.

## 1.2.2 Spectroscopy

UV-VIS-NIR absorption spectroscopy is a useful tool for investigating electronic transitions in SWNTs. As described earlier, absorption occurs at wavelengths corresponding to electron transition between symmetric van Hove singularities, shown in Figure 2. This information is used to gain insight into the quality of the  $sp^2$  lattice, as damaged SWNTs will not have the same electronic transitions. Wavelengths of light over the UV-VIS-NIR region (200 – 1400 nm) of the electromagnetic spectrum can give insight into the electronic transitions and quality of  $sp^2$  lattice. However, this technique cannot determine the chemical structure of a carbon nanotube. In order to probe the chemical structure of a SWNT, FTIR is often employed. FTIR instruments use longer wavelengths of light than UV-VIS-NIR spectrophotometers, 2,500 – 25,000 nm, to cause vibrational excitations of bonds in molecules. The absorption of specific frequencies of IR light is measured to gain information about vibrations of molecules and chemical bonds in SWNTs. Vibrations of molecules can be determined by measuring absorption of light, as in FTIR spectroscopy, or scattered light, as used in Raman spectroscopy. Raman spectroscopy monitors the changes in energy from inelastically scattered photons, after generating vibrational excitations in molecules. Monochromatic light is focused on a sample and the photons interact with vibrations of molecules in the sample, losing or gaining energy in the process. The scattered photons with new energy values, which are “shifted” up or down from the incident laser wavelength is measured. While FTIR spectroscopy offers information about the chemical structure and functional groups present on SWNTs, Raman spectroscopy gives information about the macrostructure of the CNTs. SWNTs have unique vibrations that can be characterized by

Raman spectroscopy; a sample Raman spectrum of SWNTs excited with a 633nm laser is shown in Figure 3.

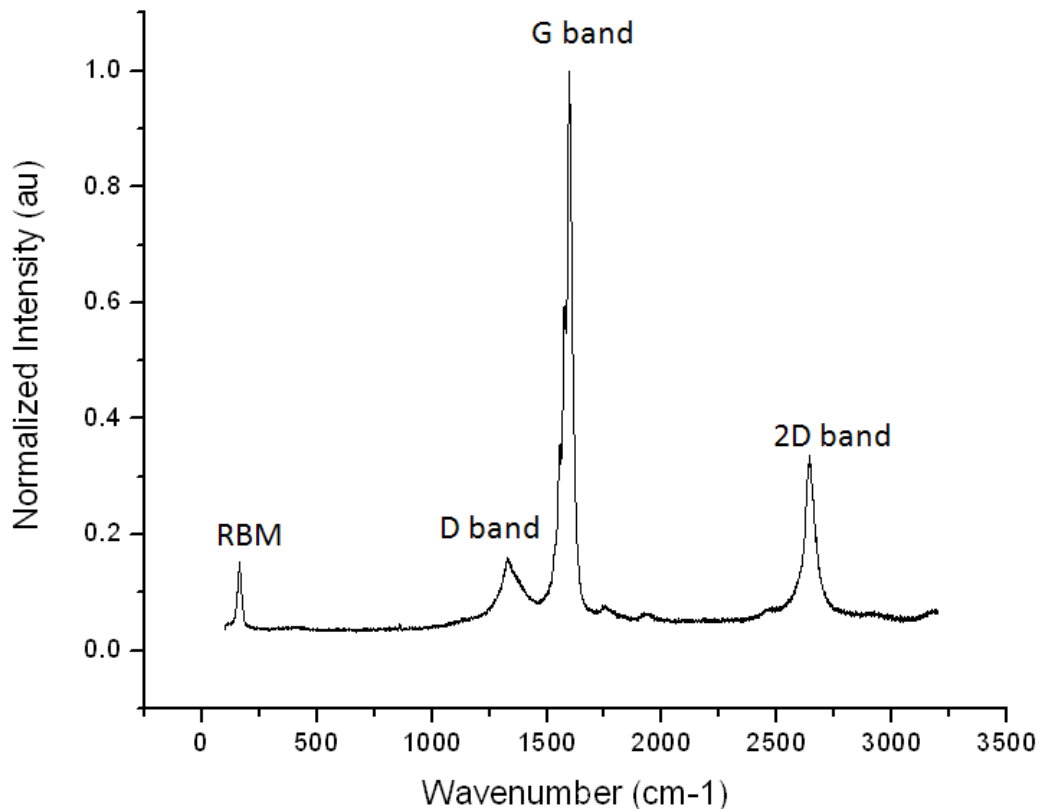


**Figure 3 Raman Spectrum of HiPco SWNTs**

The most intense peak, the G line, located at  $\sim 1582\text{cm}^{-1}$ , originates from tangential oscillations of carbon atoms. The D line found at  $\sim 1380\text{ cm}^{-1}$ , is a result of defects induced in the  $\text{sp}^2$  lattice of the nanotubes. The D/G ratio is often used to give a comparison of the defect density in SWNTs, however this value can be misleading because the coalescence of defects can decrease the D/G ratio.<sup>19</sup> Furthermore, this value does not give information about the spatial location of the defects. The radial breathing mode (RBM) is located between  $\sim 100 - 200\text{ cm}^{-1}$ , and is a symmetric expansion of the diameter of a SWNT. While D and G bands will appear in the

Raman spectrum of any structure that contains a large  $sp^2$  network, such as graphite, the RBM is inherent to the geometry of carbon nanotubes, and thus can be used to test for the presence of SWNTs. The 2D band is a second order phonon process which is highly dependent on the electronic structure of surrounding materials. It can be used to determine curvature of carbon nanotubes.<sup>20</sup>

### 1.2.3 Enzymatic Oxidation of SWNTs

In addition to their advantageous electronic properties, CNTs have shown promise as a drug delivery platform based on their small size, large surface area, and inert chemical nature.<sup>21</sup> However, they have also been shown to induce cytotoxic effects.<sup>22</sup> Therefore, it is desirable to find ways to make these materials biocompatible. One method to achieve this goal, involves oxidizing CNTs, however, chemical oxidation requires the use of harsh chemicals. An environmentally friendly, alternative route to oxidation of CNTs using enzymes has been investigated. Horseradish peroxidase, a plant enzyme obtained from the root of horseradish, contains 308 amino acid residues and an iron (III) protoporphyrin IX heme group, shown in Figure 5 (a), has demonstrated the ability to oxidize organic substrates and carbon based nanomaterials, including SWNTs.<sup>23-25</sup> HRP follows a peroxidase cycle, where the oxidation state of the iron atom in the heme group is increased from (III) to (IV), and a porphyrin-based cation radical is formed after reacting with hydrogen peroxide, as shown in Figure 4 (b). The iron(IV) porphyrin cation radical state of the enzyme, known as Compound I, oxidizes a substrate by two, one electron oxidation steps, converting to Compound II, and then finally back to the native iron(III) form of HRP.<sup>26</sup> Compounds I and II have redox potentials of 0.941 and 0.960, respectively.<sup>27</sup> While HRP is capable of oxidizing organic compounds, the shape of the

substrate is an important factor in whether the substrate can be oxidized. Due to the presence of residues there are specific binding sites and geometries needed for interaction of a substrate with the reactive heme center in one of the intermediate forms of HRP. The structure of HRP plays an important role in peroxide catalysis and distal heme pocket residues, Arg38 and His42, are needed to stabilize the formation of Compound I through hydrogen bonding.<sup>26</sup> Substrate oxidation occurs at the edge of the heme group where an opening is found between residues.<sup>28</sup> This is illustrated in Figure 5, showing the interaction of the heme group and neighboring residues with an organic substrate, ferulic acid (FA). The presence of oxygen functionalities in the organic substrate also influences the ability of HRP to oxidize the substrate. It has been shown that oxygen groups on the surface of SWNTs may decrease the distance between the SWNT and the reactive heme edge, allowing oxygenated SWNTs to be oxidized but not pristine SWNTs.<sup>25</sup>

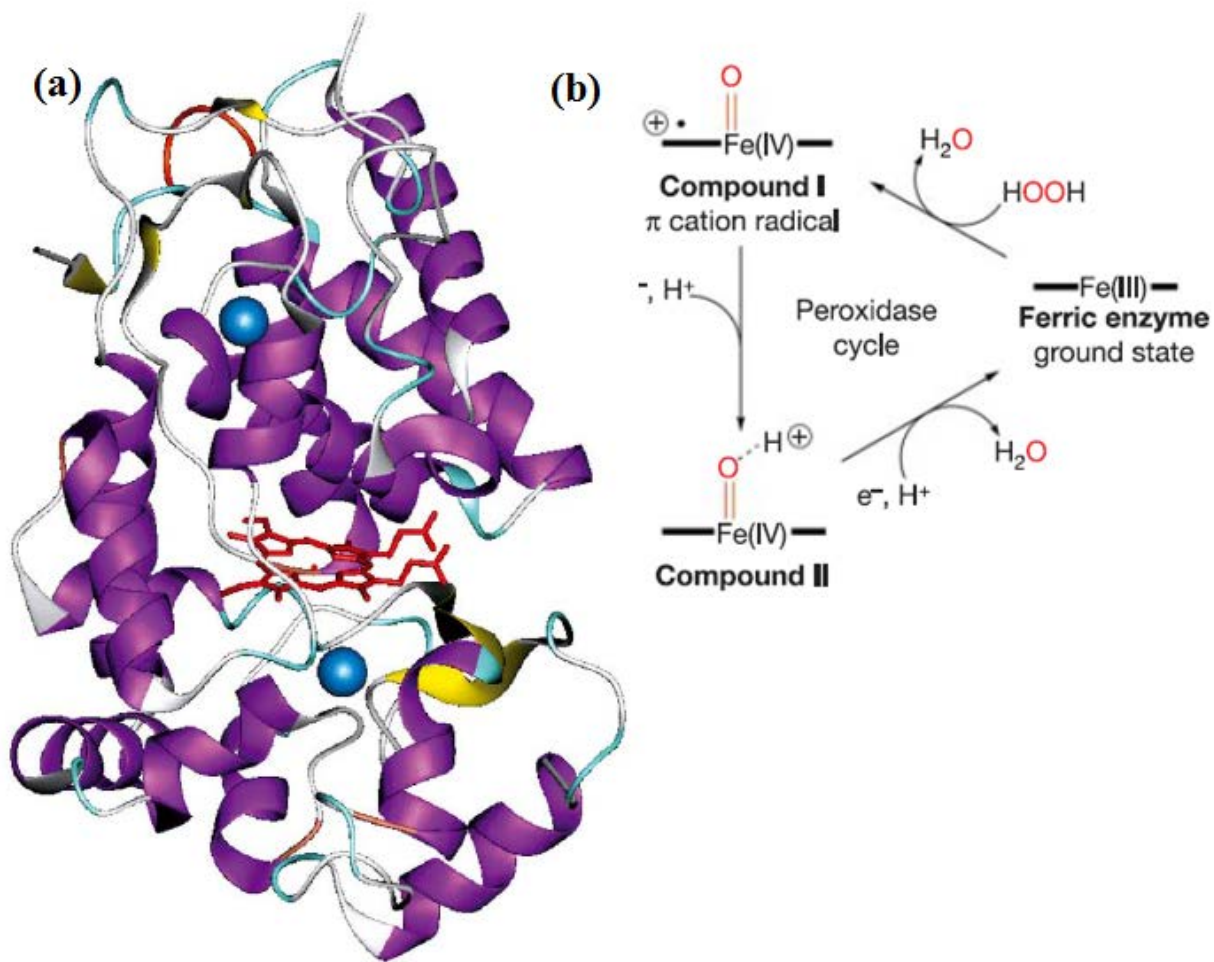


**Figure 4 Horseradish Peroxidase (HRP)** (a) structure of HRP adapted from reference 23 (b) peroxidase cycle oxidation involving HRP adapted from reference 26

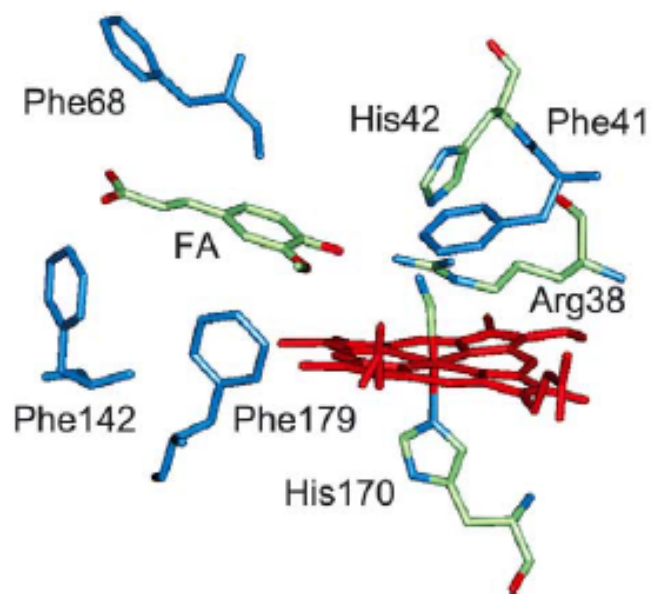


**Figure 5** HRP binding site depicting amino acid residues surrounding heme catalytic center adapted from reference 23

## 1.2.4 TiO<sub>2</sub> – Carbon Nanomaterial Photocatalysis

TiO<sub>2</sub> is a popular photocatalyst due to its low cost, nontoxicity, and small band gap. TiO<sub>2</sub> most commonly exists in 2 crystal structures: anatase and rutile, whose band gaps are 3 and 3.2eV, respectively.<sup>29</sup> Due to the small band gaps, electrons are capable of being excited from the valence band to the conduction band using UV light. Generated electron – hole pairs can then react with other molecules, reducing or oxidizing them, as shown in Figure 7 (a). In order to reduce or oxidize a substrate, the electron – hole pair must exist long enough to come into contact with the substrate. The major limitation to photocatalysis is electron – hole recombination, where excited electrons return to the valence band without reacting with a substrate. Doping TiO<sub>2</sub> with metals has shown to improve photocatalytic efficiency by slowing electron – hole recombination. Metals, such as copper and platinum, have available energy levels at energies lower than those of excited electrons in TiO<sub>2</sub>.<sup>30</sup> As a result, excited electrons will flow into the metal, which acts as an “electron sink,” as shown in Figure 6 (b). After transferring to the metal, electrons will not recombine as readily with holes in the TiO<sub>2</sub> valence band. The excited electrons, can now reduce substrates that come in contact with the surface of the metal, and their left over holes can oxidize substrates on the surface of TiO<sub>2</sub>.

Photocatalytic reduction of CO<sub>2</sub> has received increasing attention lately. CO<sub>2</sub> emissions from the burning of fossil fuels are the leading cause of increased global surface temperature,  $0.74 \pm 0.18$  °C over the 20<sup>th</sup> century.<sup>1</sup> Adverse environmental effects coupled with the increasing cost of fossil fuels have spurred the desire to find clean and cheap fuel sources. Gas chromatography has shown that TiO<sub>2</sub> can photocatalyze the reduction of CO<sub>2</sub> with water to produce methane, methanol, formic acid, and formaldehyde under UV light exposure.<sup>31-33</sup> While doping of TiO<sub>2</sub> with metals has increased reduction efficiency and selectivity, however,

efficiency is still too low for practical applications. Carbon nanostructures such as nanotubes and graphene have been suggested as  $\text{TiO}_2$  dopants due to their electron storage capacity, conductivity, large surface area, and mechanical properties.<sup>30</sup> Elucidating  $\text{TiO}_2$ -carbon nanostructure interactions can give insight towards improving efficiency for  $\text{CO}_2$  photoreduction.

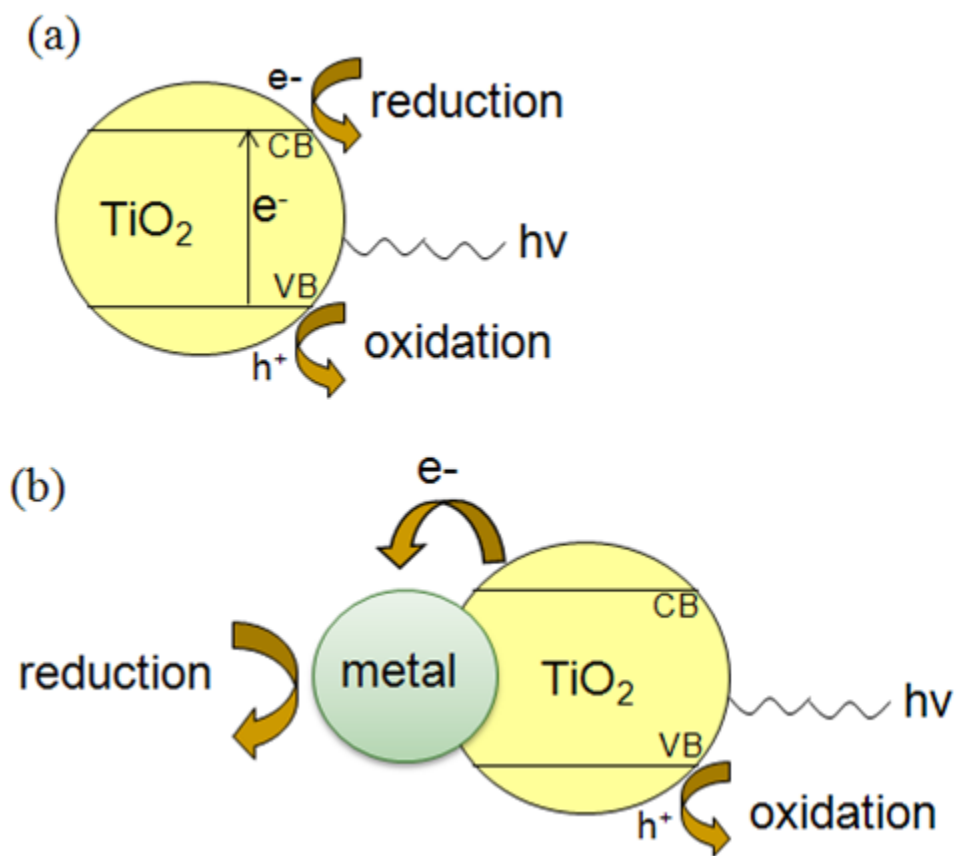


**Figure 6  $\text{TiO}_2$  photocatalysis** (a) photocatalytic oxidation and reduction on pure  $\text{TiO}_2$  and (b) metal doped  $\text{TiO}_2$

## 2.0 MECHANISTIC STUDY OF THE ENZYMATIC OXIDATION OF CARBON NANOTUBES

Carbon nanotubes (CNTs) have become a popular material for integration in composite structures, electronics, and medical therapeutics.<sup>34-36</sup> As exposure to CNTs increases, there is a need to understand interactions of CNTs in the environment and with the human body. Several studies have shown possible cytotoxic effects due to carbon nanotube exposure due to their fiber structure. Nanotubes may be engulfed by cells during endocytosis, causing a rupture of the cell due to the length of the nanotube.<sup>37</sup> It has been demonstrated that certain enzymes have the ability to oxidize and shorten carboxylated CNTs.<sup>24-25,38-39</sup> The oxidation and shortening of carbon nanotubes using enzymes could provide a pathway to utilize the beneficial properties of CNTs while limiting their toxic side effects to humans and the environment. Here, the mechanism and interaction between chemically oxidized SWNTs and horseradish peroxidase, a common plant enzyme known to oxidize organic substrates, is investigated.

The material contained in this chapter will be included in a manuscript (currently in preparation to be submitted).

**List of Authors:** Brian Barth, Chiu Cheuk Fai, Yanan Chen and Alexander Star

**Author Contributions:** BB and AS designed the experiments. CNT oxidation, spectroscopy, and microscopy were conducted by BB. Spectroscopy and photoluminescent mapping were conducted by CCF. CNT oxidation was performed by YC.

## 2.1 EXPERIMENTAL DETAILS

### 2.1.1 Chemical Oxidation and Characterization of SWNTs

Purified high pressure carbon monoxide (HiPco) SWNT's<sup>40-41</sup> purchased from NanoIntegris Inc. (Skokie, IL) were chemically oxidized using two different methods described below: sulfuric acid/nitric acid and piranha (sulfuric acid/30% hydrogen peroxide) solution treatment.

#### *Sulfuric/Nitric Acid Oxidation*

SWNTs (10 mg) were sonicated in sulfuric acid/nitric acid solutions (15 mL H<sub>2</sub>SO<sub>4</sub>, 5 mL HNO<sub>3</sub>) for 3 hours 50 minutes at 40 °C. Two separate batches were made.

#### *Piranha Solution Oxidation*

SWNTs (10 mg) were stirred in piranha solutions (8 mL, H<sub>2</sub>SO<sub>4</sub>, 2 mL 30% H<sub>2</sub>O<sub>2</sub>) for 18 hours at room temperature.

Oxidized SWNT samples were diluted with excess deionized (DI) water, vacuum filtered, washed with DI water several times, and collected on separate polytetrafluoroethylene (PFTE)

filter papers to form a thin films known in literature as bucky paper.<sup>42</sup> As prepared sections of the bucky papers were used for characterization by Raman and FTIR spectroscopy. One mg pieces were cut from each sulfuric/nitric oxidized CNT and piranha solution oxidized CNT bucky paper and each piece was sonicated for 40 minutes at room temperature in DI water (10 mL). The resulting suspensions of sulfuric/nitric acid and piranha solution oxidized HiPco SWNTs were centrifuged (3,500 RPM, 20 minutes), and the supernatant of dispersed SWNT samples were collected and used for UV-VIS-NIR absorption spectroscopy, TEM, and photoluminescent (PL) mapping.

#### *UV-VIS-NIR Spectroscopy*

Measurements of dispersed SWNTs were taken using a Perkin Elmer Lambda 900 spectrophotometer, over the wavelength range 200 – 1300 nm. Sodium cholate was used as a surfactant in UV-VIS-NIR spectroscopy studies for the 0.1 and 1.54 mg HRP oxidized samples.

#### *Raman Spectroscopy*

Raman spectra were excited with a 633 nm laser and measurements were performed using the Renishaw InVia Raman microscope. Aliquots (~0.1 mL) of suspended SWNTs were dropcast on a glass slide and allowed to dry in ambient conditions overnight, forming aggregates of SWNTs. Scans were carried out at 10% laser power, with 10 second accumulation time over the range of 100 – 3200  $\text{cm}^{-1}$ . Spectra were taken from multiple locations on SWNT aggregates, and the results were normalized to the most intense peak and averaged, in accordance with published procedures.<sup>43</sup>

### *TEM and Histogram Determination*

Dispersed SWNTs (6  $\mu\text{L}$ ) were dropcast on lacey carbon coated copper grids (Pacific-Grid Tech) and allowed to dry overnight. Analysis was performed using an FEI Morgagni TEM with 80 keV electron beam. Approximately 100 nanotubes per sample observed in microscope images were measured and length distributions were recorded.

### *FT-IR Spectroscopy*

Sections of the bucky paper (0.5 mg) were cut and ground with KBr using a mortar and pestle. The ground mixture was dried with KBr in a vacuum oven (Fischer Scientific vacuum oven model 285, -100 kPA, 75  $^{\circ}\text{C}$ ) for 4 hours. Analysis was performed using a Shimadzu IR-Prestige 21 Fourier transform infrared spectrophotometer (32 scans, 400-4000  $\text{cm}^{-1}$  range). Data manipulation included: atmospheric correction, multipoint baseline correction, and Kubelka Munk manipulation.

### *Photoluminescent Mapping*

Sodium cholate was added to SWNT suspensions (1% by mass) and the suspensions were sonicated (20 minutes). Excitation wavelength was scanned from 580 to 800 nm in 5 nm increments, and emission was detected from 900 to 1300 nm in 2 nm increments.

### 2.1.2 Enzymatic Oxidation of SWNTs Using Horseradish Peroxidase

Dispersed SWNT samples, carboxylated using a sulfuric/nitric acid mixture and piranha solution, were each combined with three different quantities of HRP (0, 0.1 and 1.54 mg) to compare amount of enzyme needed for enzymatic oxidation with previously published works.<sup>25</sup> The samples were incubated for 24 hours at room temperature on a shaker. Control experiments were performed with no HRP added to verify the effect of HRP on carboxylated HiPco SWNTs. After the incubation period, hydrogen peroxide (0.089 M, 4  $\mu$ L) was added daily to each carboxylated HiPco SWNT sample:

- (1) Sulfuric/Nitric acid oxidized HiPco SWNTs + 1.54 mg HRP
- (2) Sulfuric/Nitric acid oxidized HiPco SWNTs + 0.1 mg HRP
- (3) Sulfuric/Nitric acid oxidized HiPco SWNTs (no HRP)
- (4) Piranha solution oxidized HiPco SWNTs + 1.54 mg HRP
- (5) Piranha solution oxidized HiPco SWNTs + 0.1 mg HRP
- (6) Piranha solution oxidized HiPco SWNTs (no HRP)

The six samples were characterized periodically over a 49 day period using UV-VIS-NIR spectroscopy, TEM, and Raman spectroscopy, and PL mapping, as described previously.

## 2.2 RESULTS AND DISCUSSION

### 2.2.1 Characterization of Chemically Oxidized SWNTs

Characterization data for two batches of HiPco SWNTs oxidized by sulfuric/nitric acid treatment is shown in Figures 7 and 8. TEM was used to determine average SWNT length and standard deviation of ~308 nm and ~120 nm, respectively, for both batches, from a sample size of 100 CNTs. Raman, UV-VIS-NIR, and FTIR spectroscopy were used to investigate the homogeneity of the  $sp^2$  network. Through calculations of the ratio of two characteristic peaks, the D and G bands, which appear at approximately  $1390\text{ cm}^{-1}$  and  $1580\text{ cm}^{-1}$ , respectively, Raman spectroscopy offers valuable information about defect sites present in the SWNT lattice. The large D/G ratios of 0.491 and 1.01 indicate the presence of many defects, most likely created by adding oxygen functionalities to the  $sp^2$  carbon network during acid oxidation.<sup>44</sup> UV-VIS-NIR spectroscopy was used to investigate electronic transitions in metallic and semiconducting SWNTs. The spectra in Figures 7 (c) and 8 (c), show small metallic (~400 – 600 nm) and semiconducting (~ 550 – 1600 nm) absorption bands, which could be the result of the destruction of the  $sp^2$  network during the acid oxidation treatment and functionalization of the lattice with oxygen groups.

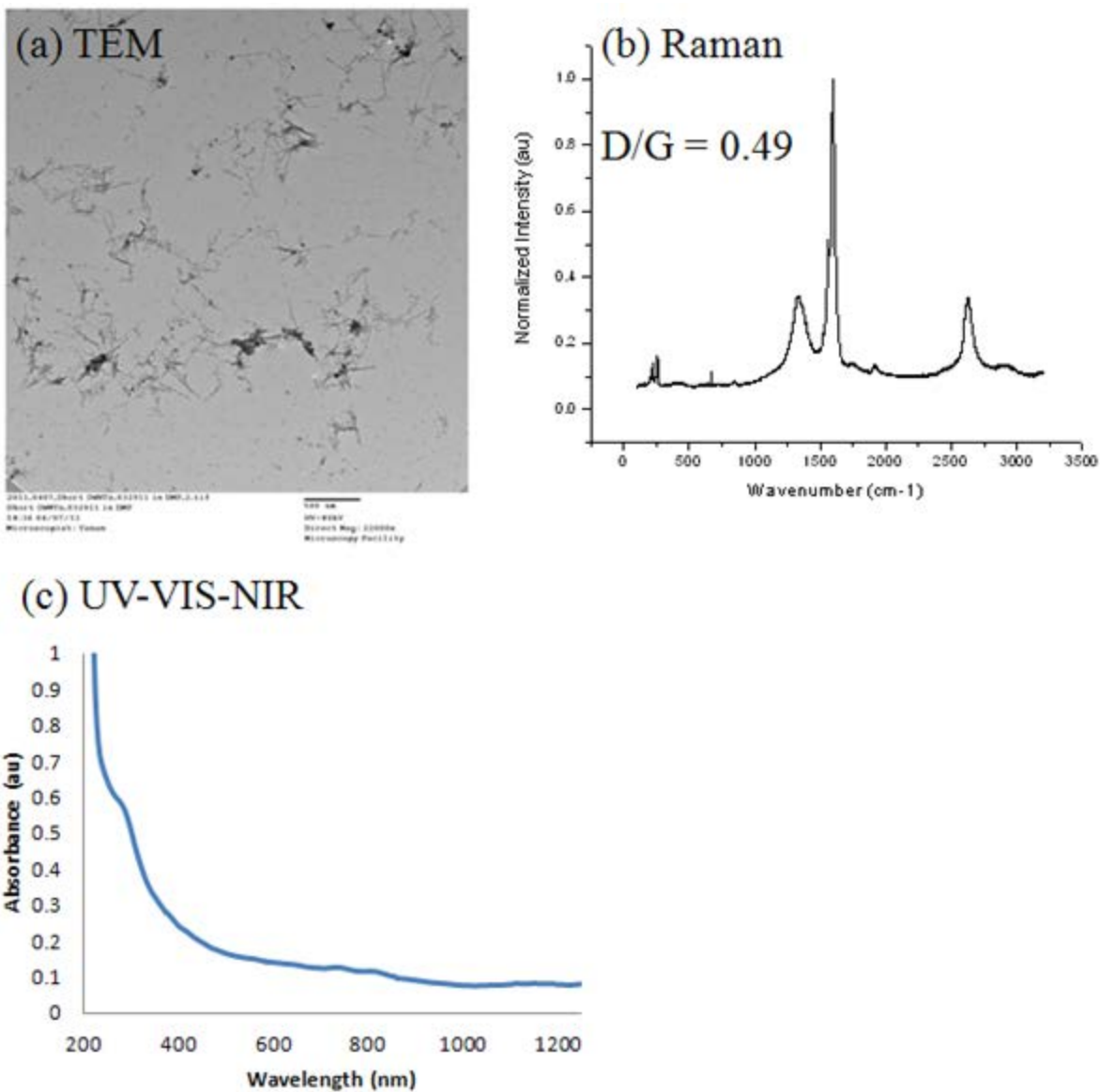


**Figure 7** Characterization of  $\text{H}_2\text{SO}_4 / \text{HNO}_3$  oxidized HiPco SWNTs (batch 1) (a) TEM image (b) Raman spectrum (c) UV-VIS-NIR spectrum

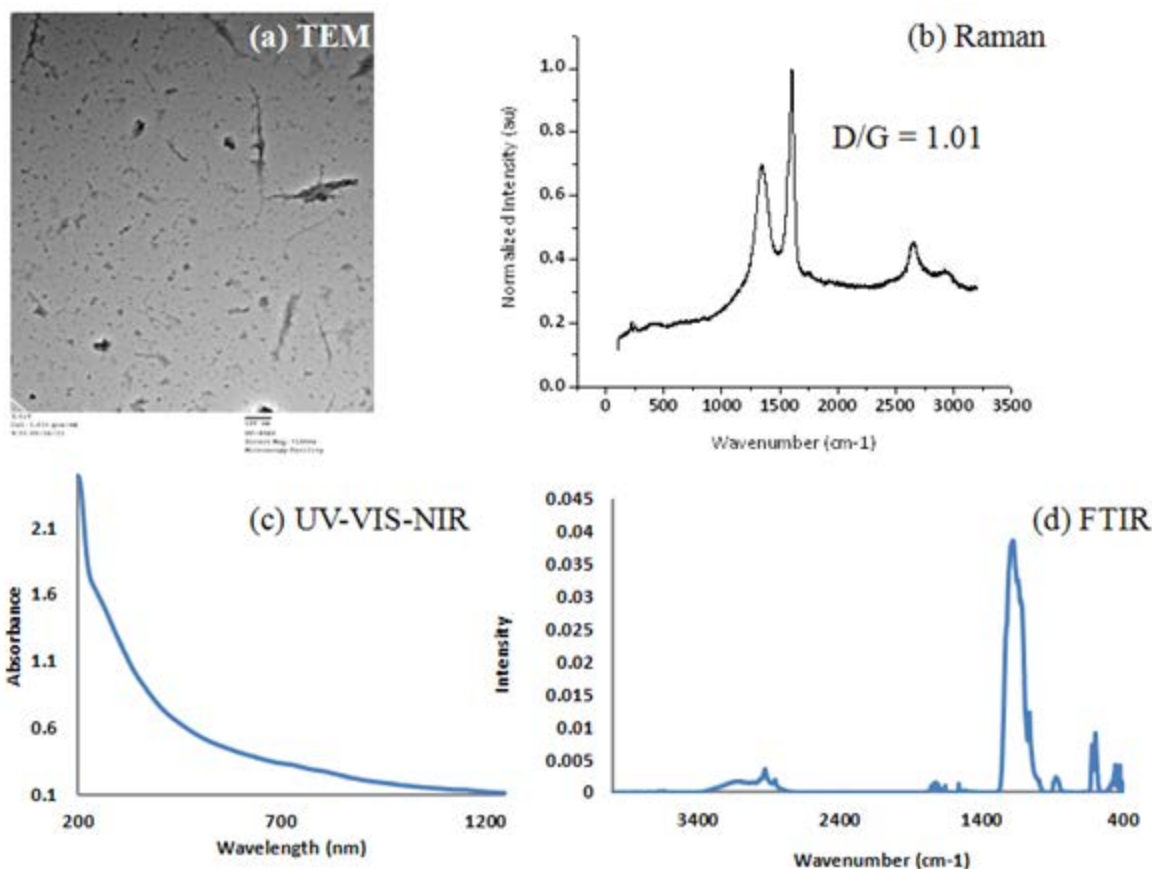


**Figure 8** Characterization of  $\text{H}_2\text{SO}_4 / \text{HNO}_3$  oxidized HiPco SWNTs (batch 2) (a) TEM image (b) Raman spectrum (c) UV-VIS-NIR spectrum (d) FTIR spectrum

Due to similar microscopic and spectroscopic results, the two batches can be considered similar. The presence of oxygen functionalities is confirmed using FTIR spectroscopy, illustrated in Figure 8 (d). There is a strong IR signal at  $\sim 1100 \text{ cm}^{-1}$  which corresponds to C – O stretching vibration from alcohol, carboxylic acid, ether, or ester functional groups. A weak, broad signal is located from  $\sim 3200 - 2800 \text{ cm}^{-1}$ , with 2 sharp peaks appearing at  $\sim 2900 \text{ cm}^{-1}$ , overlapping the broad band. The broad peak corresponds to an O – H stretching vibration possibly from carboxylic acid groups (O – H stretch from alcohols occur at closer to  $\sim 3500 \text{ cm}^{-1}$ ) and the sharp peaks at  $2900 \text{ cm}^{-1}$  correspond to C – H stretching vibrations, which may have been introduced

during the oxidation process.<sup>45</sup> There is a C = O band at  $\sim 1735\text{ cm}^{-1}$ . Characteristic SWNT C = C vibrations are located at  $\sim 1560, 850\text{ cm}^{-1}$ .<sup>46</sup>

Characterization data for HiPco SWNTs oxidized by piranha solution treatment is shown in Figure 9. HiPco SWNTs treated with piranha solution have a length distribution with an average of  $\sim 550\text{ nm}$  and a standard deviation of  $\sim 214\text{ nm}$  determined from TEM images, shown in Figure 9 (a). The D/G ratio in the Raman spectrum, in Figure 9 (b) is 0.19, smaller than the values of 0.49 and 1.01 for sulfuric/nitric acid oxidized HiPco SWNTs. The UV-VIS-NIR spectrum in Figure 9 (c) shows a more prominent band structure for metallic and semiconducting SWNTs for the piranha oxidized than the sulfuric/nitric acid oxidized HiPco SWNTs. These results indicate a more “pristine”  $sp^2$  lattice. The FTIR spectrum has a strong peak at  $\sim 1556\text{ cm}^{-1}$  which could be resulting from a C = C bending vibration and a broad, weak peak centered at  $\sim 3450\text{ cm}^{-1}$  that could be due to an O – H stretching vibration found in alcohols. There is no evidence of an intense peak at  $\sim 1100\text{ cm}^{-1}$ , which is characteristic of C – O stretching. There are also 2 peaks at  $\sim 2900\text{ cm}^{-1}$ , corresponding to a C – H stretching vibration. Visual and spectroscopic evidence indicates that HiPco SWNTs oxidized using piranha acid solution are not as heavily oxidized as HiPco SWNTs treated with sulfuric and nitric acids. The most commonly accepted mechanism for oxidative cutting of SWNT’s is a two step procedure: (1) introduction of defects into the  $sp^2$  network at random sites and (2) oxidative cutting of the SWNT around the induced defect site.<sup>46</sup>

Piranha solution treatment is not as strongly oxidizing as sulfuric/nitric acid treatment. Therefore, chemical oxidation using this piranha solution procedure can cut SWNT’s at already existing defect sites but does not readily produce new defect sites.<sup>43</sup> It has been shown that

oxidation of carbon nanotubes by piranha solution, introduces few carboxylic acid groups, while refluxing in nitric acid adds significantly more carboxylic acid functionalities. The concentration of carboxylic acid groups per gram of carbon nanotube material was found to be 2.0 mmol/g, 3.7 mmol/g, and 1.8 mmol/g for piranha oxidized, nitric acid (refluxed) oxidized, and pristine NTs, respectively.<sup>47</sup> This is supported by our findings, which show piranha oxidized HiPco SWNTs are longer, less defective, and contain fewer oxygen functionalities than sulfuric/nitric acid oxidized HiPco SWNTs.

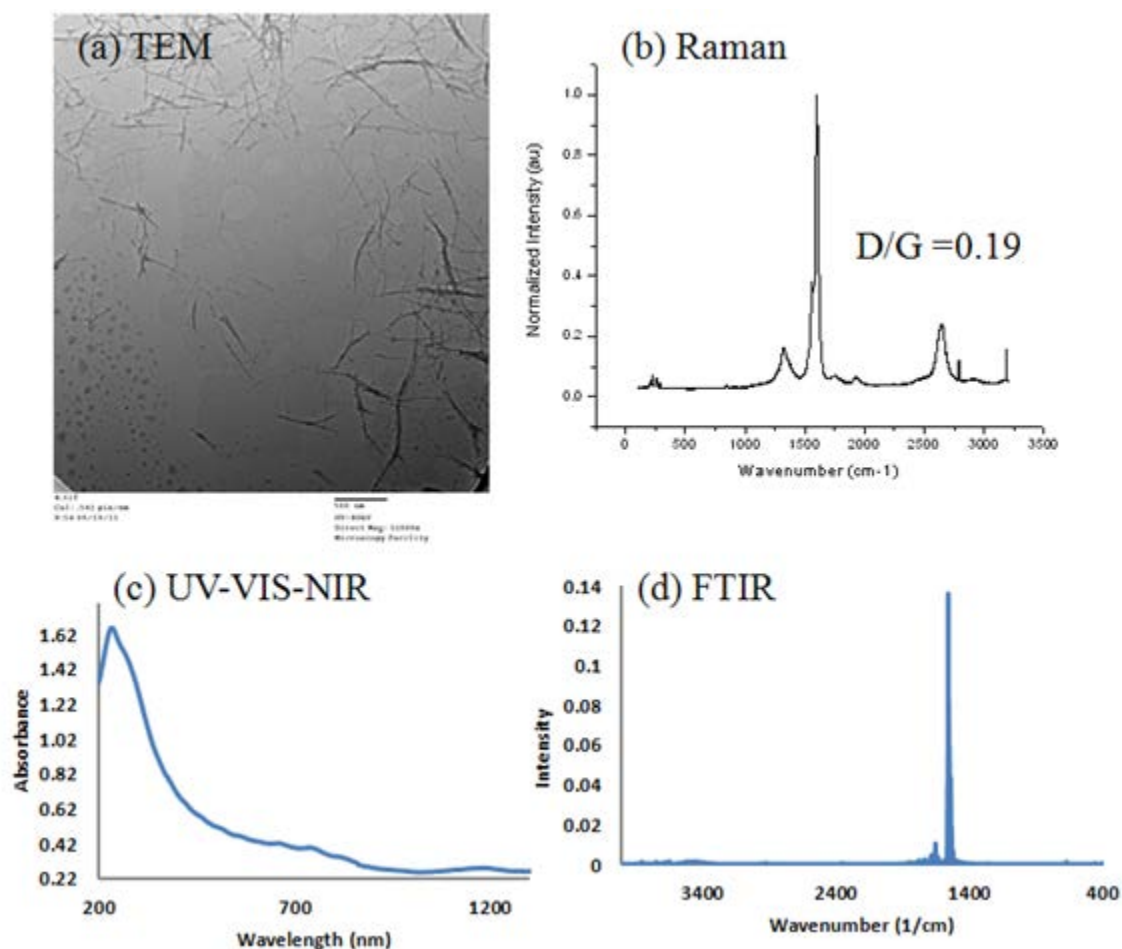


**Figure 9** Characterization of  $\text{H}_2\text{SO}_4 / \text{H}_2\text{O}_2$  oxidized HiPco SWNTs (a) TEM image (b) Raman spectrum (c) UV-VIS-NIR spectrum (d) FTIR spectrum

## 2.2.2 Enzymatic Oxidation of Chemically Oxidized SWNTs

Enzymatic oxidation of carboxylated SWNTs was performed using HRP. The iron atom in the heme group of HRP is oxidized in the presence of hydrogen peroxide, converting HRP ( $\text{Fe}^{+3}$ ) to Compound I ( $\text{Fe}^{+4}$  oxoferryl center with porphyrin cation), which oxidizes a substrate via two one-electron transfer steps, converting to Compound II ( $\text{Fe}^{+4}$  oxoferryl center) before returning to the native form of HRP ( $\text{Fe}^{+3}$ ). However, previous work has shown the ability of hemin and hydrogen peroxide to oxidize CNTs, based on reactive oxygen species (ROS) Fenton chemistry; the mechanism is shown in Figure 10.

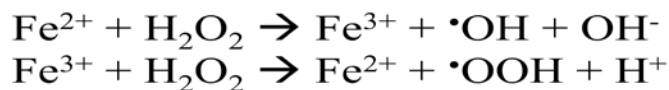


**Figure 10** Fenton catalysis

Furthermore, presence of iron catalyst particles in the HiPco SWNT samples, used in the synthesis process, may interact with hydrogen peroxide by the same mechanism. Comparisons were made between peroxidase catalyzed HRP oxidation and ROS Fenton chemistry oxidation.

Characterization data for sulfuric/nitric acid treated HiPco SWNT's after enzymatic oxidation using 0.1 and 1.54 mg HRP in comparison to oxidation without adding HRP is shown in Figure 11. Average CNT length and standard deviation of the average length (sample size 100 NTs) plotted versus time in Figure 11 (a), shows a shortening of average SWNT length over a

period of 35 days, with daily addition of hydrogen peroxide (0.089M, 4 $\mu$ L added per day), as previously shown by our group.<sup>24-25</sup> Raman spectroscopy reveals a trend of decreasing D/G ratio which is illustrated in a plot of normalized D/G versus time in Figure 11 (b). This trend can be explained by the coalescence of defects in carbon nanotube lattice, which minimizes the area of the lattice responsible for the generation of the D band.<sup>19</sup> UV-VIS-NIR spectroscopy shows reduction of absorbance in metallic and semiconducting bands after chemical oxidation, but the reappearance of some of those bands after oxidation treatment with either (1) HRP and hydrogen peroxide or (2) hydrogen peroxide, although bands appear better defined with HRP oxidation. Furthermore, there has been a separation of the S<sub>11</sub> bands in samples following HRP treatment versus as received samples, indicating oxidative treatment may have debundled some of the SWNTs. PL mapping was also used to examine the quality of the sp<sup>2</sup> network of this sample. Figure 12 shows that purified HiPco SWNT's demonstrate fluorescence because of their pristine sp<sup>2</sup> network, but chemically oxidized CNT's show no fluorescence because the conjugated network has been broken and functionalities have been imparted on the CNT, which may quench the fluorescent signal. However, after incubation with HRP for 35 days, a fluorescent signal reappears. Treating sulfuric/nitric acid oxidized HiPco SWNTs with hydrogen peroxide (without HRP) slightly increased the absorption from the S<sub>11</sub> band but showed no increase in the photoluminescent signal. HRP shows more selectivity than ROS (generated from the addition of hydrogen peroxide without HRP), since HRP would bind to highly oxygenated site on the NT, while ROS would oxidize a substrate only when it came close enough to an oxidizable site through diffusion. The return in band structure observed in UV-VIS-NIR spectroscopy as well as the photoluminescent signal could result from the removal of oxygen functionalities from the CNT by an HRP peroxidase catalyzed oxidation mechanism. The increase in absorption band

signal for the hydrogen peroxide control may have been triggered reactions between ROS and oxygenated sites. As functionalized sites are further oxidized, CO<sub>2</sub> could be removed from lattice, eliminating the presence of oxygen functionalities. Hydrogen peroxide might not be able to restore photoluminescence or optical bands as well as HRP due to the lack of selectivity.

Characterization data for piranha treated HiPco SWNT's after enzymatic oxidation using 0.1 and 1.54 mg HRP is shown in Figure 13 with a control experiment (no added HRP) shown for comparison. All three samples show similar results. The results show a slight decrease in average CNT length, a decrease in D/G ratio, little change in absorption band intensities, and no fluorescent signal for any of the samples. The decrease in length and D/G ratio can be explained by the oxidation of oxygenated sites on the CNTs. Defective portions of the CNTs were cut, making the CNTs shorter. As the defective areas coalesce, D/G ratio decreases, as previous stated. UV-VIS-NIR spectra show well defined bands but no photoluminescent signal, as shown in Figure 14. This could be due to presence of oxygen groups on the CNTs after enzymatic treatment. The weakly oxidizing piranha solution may have generated alcohol groups but few carboxylic acid groups as shown by FTIR spectra and published results.<sup>47</sup> Alcohol groups require more energy to oxidize and eventually be removed from the lattice than carboxylic groups. The presence of alcohol groups, which are more difficult to remove, could quench the fluorescent signal.

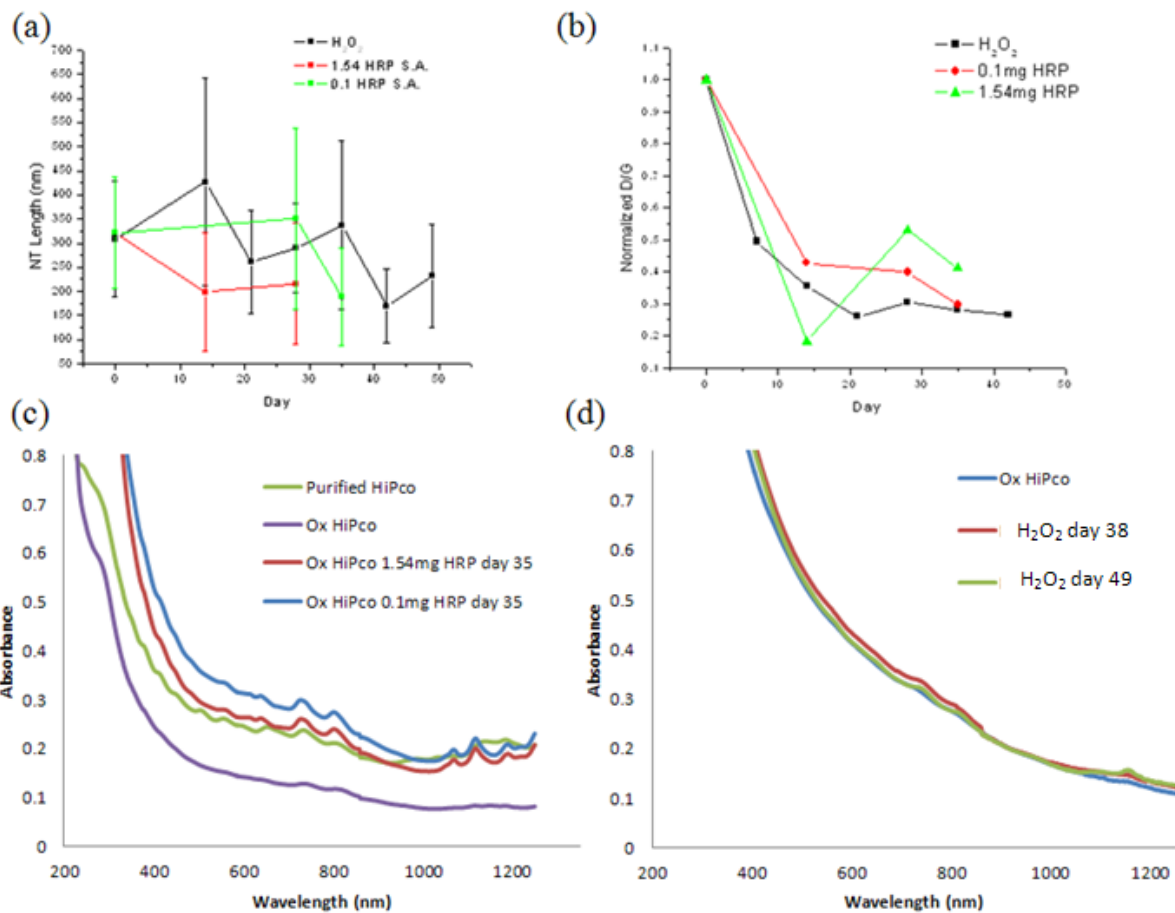


**Figure 11 Characterization of HRP treated  $H_2SO_4 / HNO_3$  oxidized HiPco SWNTs** (a) Length vs. time plot determined from TEM images (b) Normalized D/G ratio vs. time determined from Raman spectra (c) UV-VIS- NIR spectra for batch 1 samples treated with HRP and  $H_2O_2$  (d) UV-VIS-NIR spectra for batch 2 samples treated with  $H_2O_2$  (-HRP)

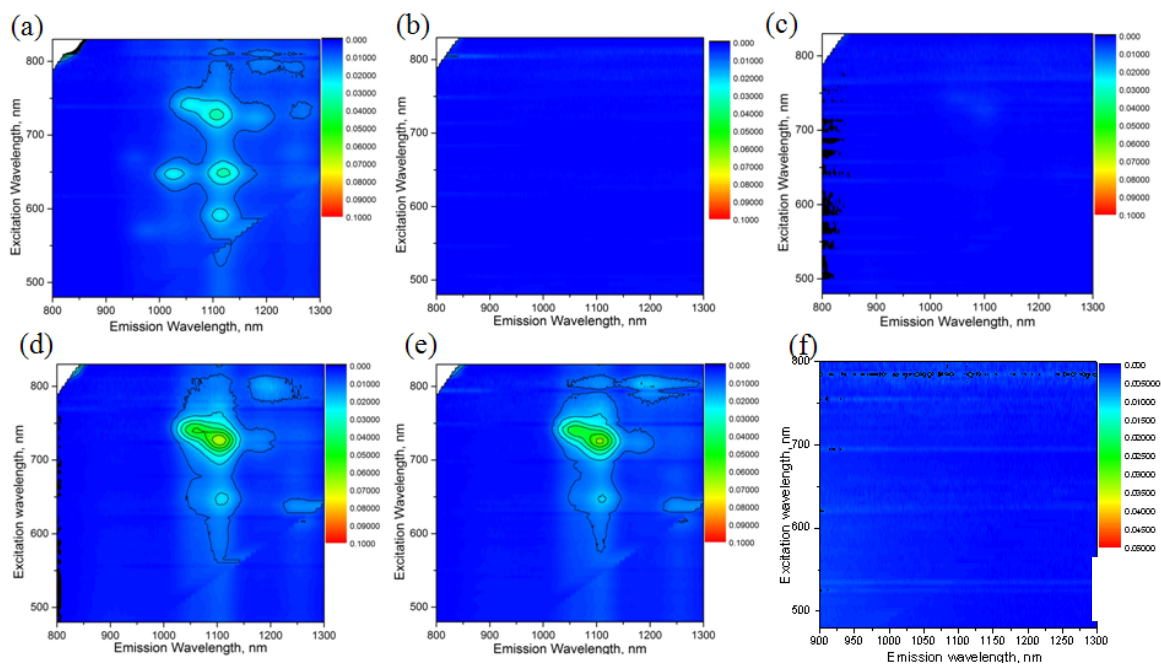


**Figure 12** PL mapping data for HRP treated  $\text{H}_2\text{SO}_4 / \text{HNO}_3$  oxidized HiPco SWNTs (a) pristine HiPco SWNTs prior to oxidative treatment (b) HiPco SWNT oxidized with sulfuric/nitric acid mixture (c) HRP (d) HiPco SWNT oxidized with sulfuric/nitric acid mixture after 35 days of  $\text{H}_2\text{O}_2$  additions while incubated with 1.54 mg HRP (e) HiPco SWNT oxidized with sulfuric/nitric acid mixture after 35 days of  $\text{H}_2\text{O}_2$  additions while incubated with 0.1 mg HRP (f) HiPco SWNT oxidized with sulfuric/nitric acid mixture after 49 days of  $\text{H}_2\text{O}_2$  (- HRP)

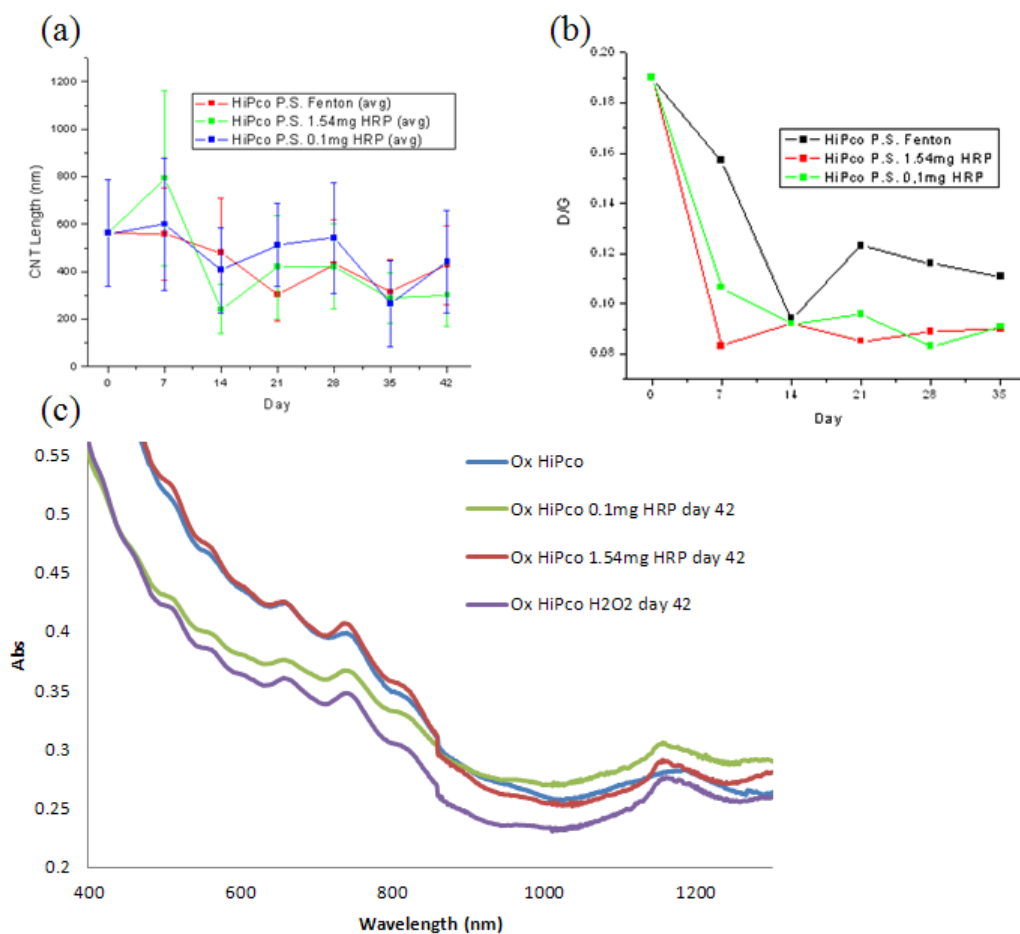


**Figure 13 Characterization of HRP treated  $H_2SO_4 / H_2O_2$  oxidized HiPco SWNTs** (a) Length vs. time determined from TEM images (b) Normalized D/G ratio vs. time determined from Raman spectra (c) UV-VIS-NIR spectra comparing oxidized SWNTs, oxidized SWNTs treated with HRP and  $H_2O_2$  for 42 days, and oxidized SWNTs treated with  $H_2O_2$  for 42 days

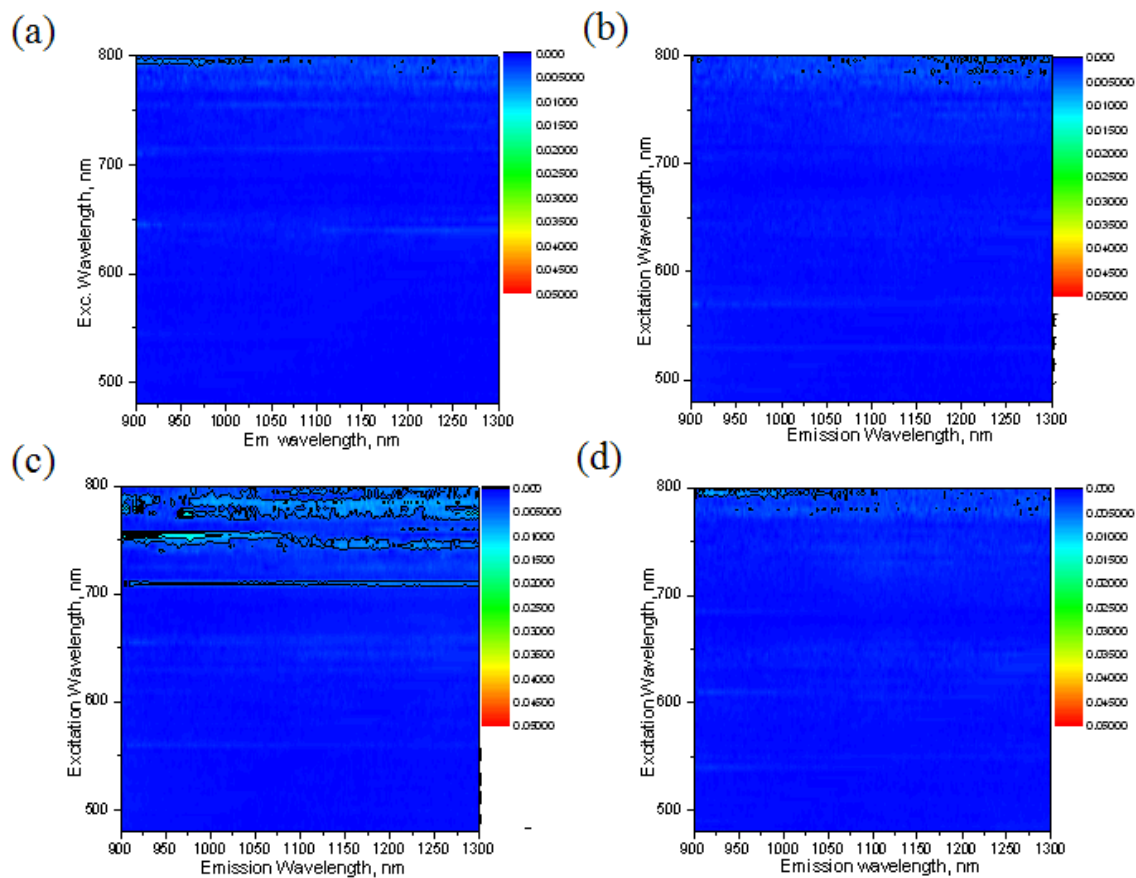


**Figure 14** PL mapping data for HRP treated  $\text{H}_2\text{SO}_4 / \text{H}_2\text{O}_2$  oxidized HiPco SWNTs (a) HiPco SWNTs oxidized with  $\text{H}_2\text{SO}_4 / \text{H}_2\text{O}_2$  (b) After 42 days of  $\text{H}_2\text{O}_2$  additions while incubated with 1.54 mg HRP (c) After 42 days of  $\text{H}_2\text{O}_2$  additions while incubated with 0.1 mg HRP (d) After 42 days of  $\text{H}_2\text{O}_2$  additions (- HRP)

## 2.3 CONCLUSIONS

HRP is capable of oxidizing highly defective, carboxylated SWNTs and restoring their optical properties. HiPco SWNTs that were heavily oxidized and showed weak absorption bands with no luminescence, were further oxidized using HRP to give shorter, less defective CNTs with well defined absorption bands and strong luminescent signal. Weakly oxidized SWNTs which were

not as defective and showed fairly well defined absorption bands gave no photoluminescent signal after HRP oxidation. HRP may be capable of oxidizing only carboxylic acid groups, which would remove CO<sub>2</sub> from the CNT lattice. It is possible that oxygen atoms in alcohol groups are not as easily removed from the lattice as oxygen atoms in carboxylic groups, due to the number of bonds between the carbon in the oxygen functional group and the lattice.<sup>48</sup> As a result, HRP is not capable of removing oxygen atoms generated by piranha solution oxidation.

### 3.0 TiO<sub>2</sub> – CARBON NANOMATERIALS PHOTOCATALYSTS

Increasing energy demands and costs have spawned interest in cheap fuel sources. Furthermore, rising global temperatures due to green house gas emissions, associated with the combustion of fossil fuels, has brought into question the environmental repercussions of using currently available fuel sources. As a result, research involving the discovery of environmentally friendly, renewable, cheap fuel sources has received much attention. One of the more promising areas of renewable energy research is CO<sub>2</sub> reduction. CO<sub>2</sub> reduction has been performed via photocatalysis using TiO<sub>2</sub> nanoparticles, however, efficiency is too low for practical application.<sup>31</sup> Efforts to improve this existing technology by doping TiO<sub>2</sub> nanoparticles with carbon nanomaterials have more recently been studied.<sup>49</sup> Here, the interaction of TiO<sub>2</sub> nanoparticles with carbon nanomaterials, for photocatalytic applications, is investigated.

The material presented in this chapter will be included in a manuscript (currently in preparation to be submitted).

**List of Authors:** Brian Barth, Yifan Tang, and Alexander Star

**Author Contributions:** BB and AS designed experiments. Synthesis experiments, spectroscopy measurements, and mass spectrometry measurements were performed by BB. Mass spectrometry measurements were performed by YT.

## 3.1 EXPERIMENTAL DETAILS

### 3.1.1 Synthesis and Characterization

Oxidized SWNTs synthesized from an electric-arc discharge method and purified using nitric acid, were purchased from Carbon Solutions, Inc. (Riverside, CA). Graphene oxide was synthesized from graphite, purchased from Sigma – Aldrich, using a modified Hummers method. Oxidized carbon nanomaterials (~1mg of GO or oxidized SWNTs) were sonicated in ethanol (15mL) for 20 min. Titanium isopropoxide (TIP, 10  $\mu$ L), a TiO<sub>2</sub> nanoparticle precursor, was added to the carbon nanomaterial suspension under vigorous stirring and allowed to stir for 2 to 24 hours. The resulting TiO<sub>2</sub> – oxidized carbon nanomaterial photocatalysts suspensions were filtered and washed with water. Photocatalyst samples were characterized by TEM. Dried photocatalyst material was sonicated (10 min) in water and dropcast on lacey carbon coated copper grids (Pacific – Grid Tech) and allowed to dry overnight. TEM images were taken using an FEI Morgagni TEM with an 80 keV electron beam. TiO<sub>2</sub> – oxidized SWNT samples were also characterized by Raman spectroscopy using a Renishaw InVia Raman microscope with a 633 nm laser. Dry TiO<sub>2</sub> – oxidized SWNT powder was placed on a glass slide for spectroscopy measurements.

### 3.1.2 Dye Degradation

Methyl orange ( $1.14 \times 10^{-4}$  M, 3ml) dye and photocatalyst material (2mg), TiO<sub>2</sub> – SWNTs, anatase TiO<sub>2</sub> nanoparticles, or P25 nanoparticles, were combined in a quartz cuvette and stirred for 30 min in the dark to establish adsorption/desorption equilibrium. The samples were

centrifuged (3,500 RPM, 10 min) to separate photocatalyst from suspended dye. The methyl orange supernatant was collected and absorbance of the dye was measured at 455nm using a Perkin Elmer Lambda 900 spectrophotometer. Following absorbance measurements, the dye and photocatalyst material were recombined. The recombined samples were illuminated with a 100W, 365 nm lamp, while being stirred, for 30 min intervals. Following each 30 min interval, the samples were centrifuged and absorbance of the supernatant was measured, as previously described.

### **3.1.3 CO<sub>2</sub> Reduction**

CO<sub>2</sub> reduction experiments were carried out according to published procedures.<sup>31</sup> One end of a tube was attached to a CO<sub>2</sub> tank and the other was inserted into the bottom of a sealed vial containing water. A second tube was inserted into the headspace of the sealed vial containing water, with the other end inserted into a second sealed quartz vial containing dry TiO<sub>2</sub> – oxidized SWNT photocatalyst powder (10mg). Another tube was inserted into the sealed vial containing the TiO<sub>2</sub> – SWNT photocatalyst, connecting this vial to an Ametek Proline mass spectrometer (MS) for continuous measurements. A 100W, 365 nm UV lamp was positioned facing the sealed vial containing the photocatalyst. The schematic for this setup is illustrated in Figure 15. Water saturated CO<sub>2</sub> was passed through the vial containing the photocatalyst material. Once the air in the headspace of the sealed vial containing photocatalyst had been replaced with CO<sub>2</sub>, as confirmed by MS, the photocatalyst and CO<sub>2</sub> were irradiated with UV light. Continuous spectra were taken for 3 hours, and m/z was plotted versus intensity for different times.

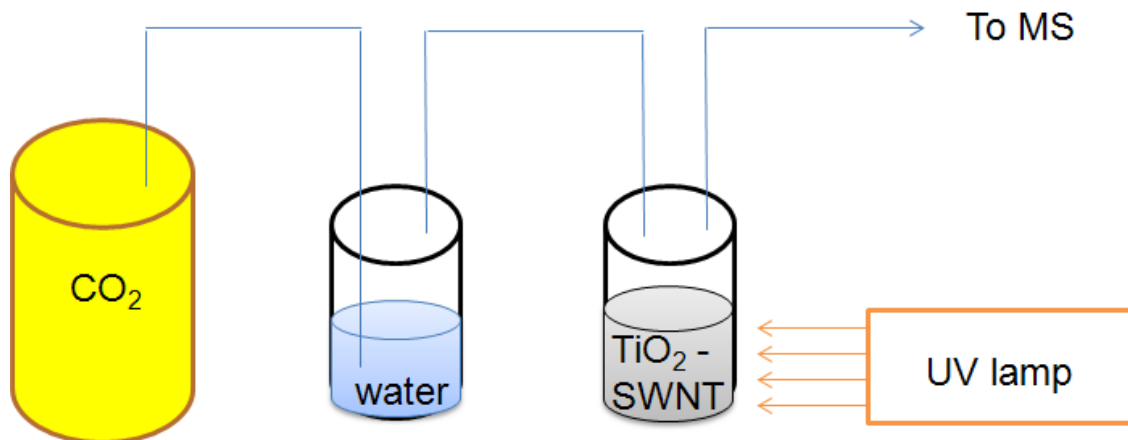
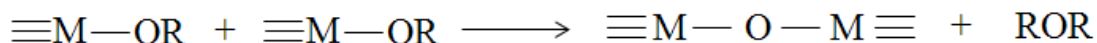


Figure 15 CO<sub>2</sub> reduction experimental design

## 3.2 RESULTS

### 3.2.1 Synthesis and Characterization

A non-aqueous sol gel synthesis route for metal oxide nanoparticles was used because it offers the advantage of better control of nanoparticle size and crystallinity in comparison to the aqueous sol gel route. The use of alcohols instead of water, can provide a source of oxygen for metal oxide formation (oxygen may also come from the metal alkoxide precursor), while slowing reaction rates, due to the moderate reactivity of the C – O bond found in alcohols versus the high reactivity of the H – O bond in water. The slower reaction rates improve the homogeneity of the metal oxide crystalline structure and particle diameter. Non-aqueous sol gel synthesis of TiO<sub>2</sub> nanoparticles most likely proceeds by ether elimination, shown in Figure 16, where two metal alkoxides react to form a metal-oxygen-metal bond and form an organic ether.<sup>50</sup>



**Figure 16 Ether elimination**

TiO<sub>2</sub> appears to form a coating around the NTs, as can be seen by the appearance of a core-shell structure, where certain segments of NTs have a much larger diameter than others, as shown in Figure 17 (a). TiO<sub>2</sub> – GO samples show the formation of TiO<sub>2</sub> nanoparticles mainly on the edges of the GO flakes, as shown in Figure 17 (b). It has been established that TiO<sub>2</sub> nanoparticles interact with oxygen containing functional groups, as illustrated in Figure 18, which is why oxidized carbon nanomaterials were used for doping TiO<sub>2</sub>.<sup>51</sup> This interaction would concentrate TiO<sub>2</sub> nanoparticles near functional groups on GO, which are known to be mainly at the edges of the flakes, in accordance with TEM images. Raman spectroscopy was used to verify the crystalline phase of the TiO<sub>2</sub> in the TiO<sub>2</sub> –SWNT sample. Although core – shell structures are identifiable on TEM, there were no characteristic peaks for TiO<sub>2</sub> anatase or rutile crystalline phases, as shown in Figure 19. Amorphous TiO<sub>2</sub> gives very weak, broad bands which may be indiscernible against the SWNT spectrum.<sup>52</sup>

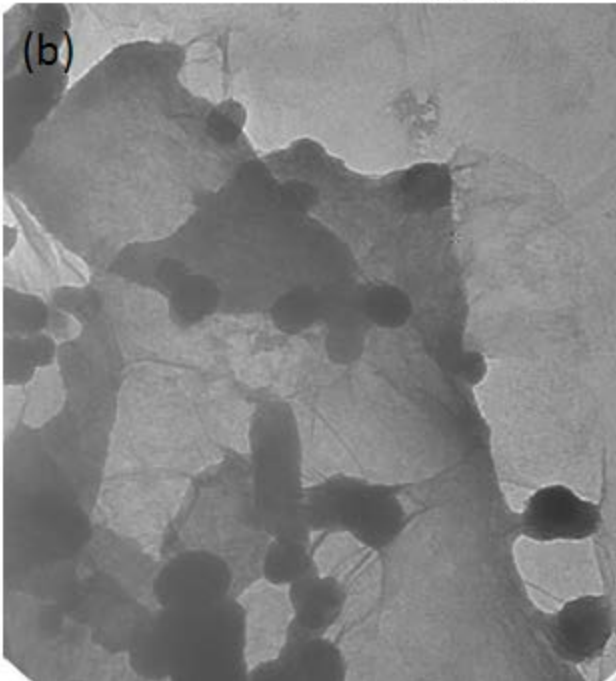
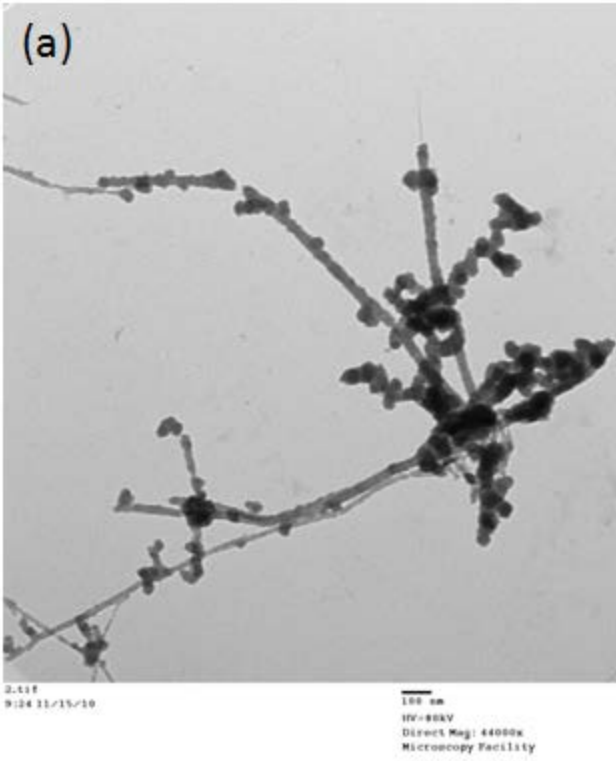


**Figure 17 TEM images of TiO<sub>2</sub> – carbon nanomaterials (a) TiO<sub>2</sub> – SWNTs (b) TiO<sub>2</sub> – GO**

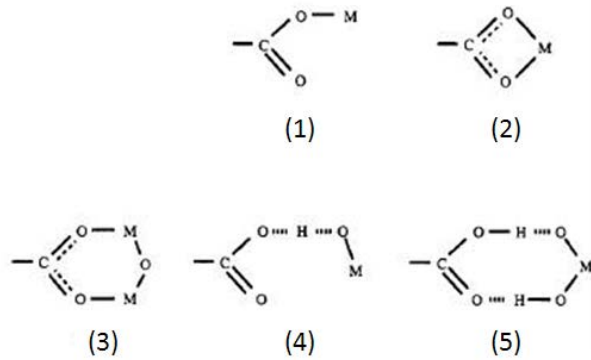


**Figure 18 TiO<sub>2</sub> – surface functional group interactions** five possible interactions between TiO<sub>2</sub> and surface functional groups (Ti atom is represented in these diagrams as M) adapted from reference 50

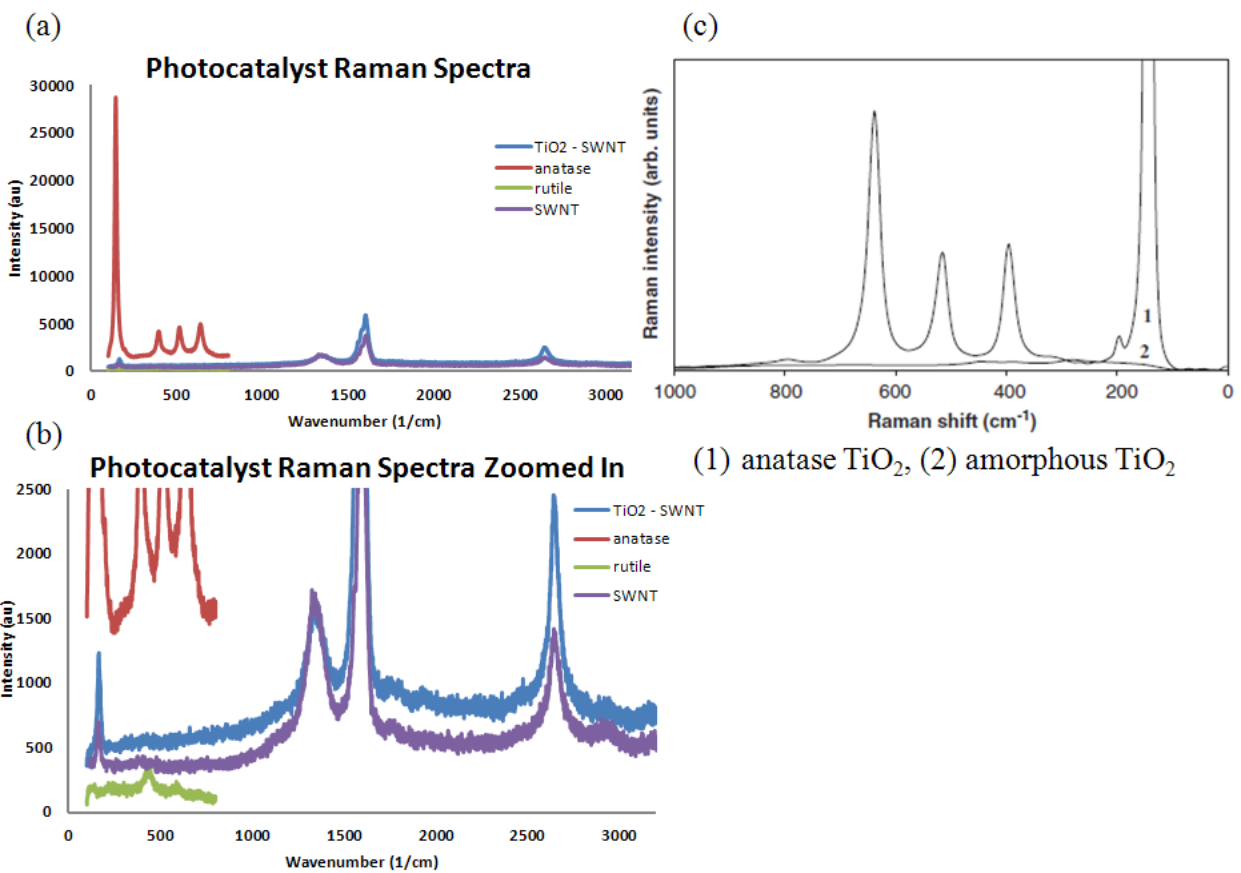


**Figure 19 TiO<sub>2</sub> Raman spectra** (a) Raman spectra of TiO<sub>2</sub> photocatalysts and SWNTs (b) zoomed in view of (a) (c) Raman spectra of anatase and amorphous TiO<sub>2</sub> adapted from reference 51

### 3.2.2 Dye Degradation

Photocatalytic efficiency of TiO<sub>2</sub> – carbon nanomaterial photocatalysts can be easily compared by how well they can oxidize organic dye under UV light exposure. Methyl orange, a common azo dye with a bright yellow-orange color, whose structure is shown in Figure 20, can be oxidized by TiO<sub>2</sub> to give colorless products.<sup>53</sup> Synthesized photocatalyst materials were compared with commercial TiO<sub>2</sub>, anatase and P25 nanoparticles.

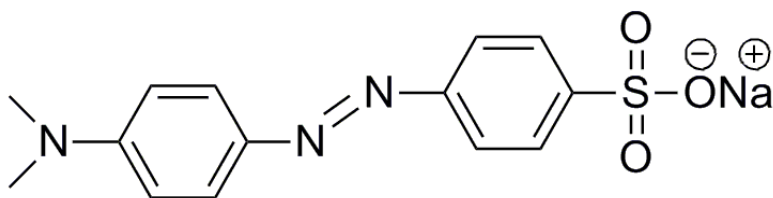


Figure 20 Structure of methyl orange

Figure 21 shows the absorbance of dye versus time for three different photocatalysts, two TiO<sub>2</sub> – SWNT samples, and two commercial TiO<sub>2</sub> samples with different crystal structure. P25 TiO<sub>2</sub> nanoparticles are a composite containing 20% rutile and 80% anatase TiO<sub>2</sub>. From Figure 21, it is shown that P25 TiO<sub>2</sub> nanoparticles have the highest photocatalytic efficiency. The presence of two crystal structures, has been shown to improve photocatalytic efficiency by reducing electron – hole recombination similar to metal doped TiO<sub>2</sub>. EPR studies have shown electron excitation occurs in the rutile phase (most likely because of the smaller band gap in comparison to anatase), followed by transfer to Ti<sup>3+</sup> trapping sites on the surfaces of anatase particles, which are at lower energy than the rutile conduction band.<sup>54</sup> Commercially available

anatase TiO<sub>2</sub> and synthesized TiO<sub>2</sub> – SWNT samples showed similar dye degradation performance, decreasing the absorbance of methyl orange dye by ~ 6%, while P25 caused a decrease in dye absorbance of ~ 97%.

The difference in photocatalytic activity between anatase and P25 TiO<sub>2</sub> samples indicates that electron – hole combination is probably limiting the ability of the photocatalyst to oxidize dye. Control experiments were carried out to test whether electrons in anatase TiO<sub>2</sub> are capable of being excited using a 365nm lamp. Anatase TiO<sub>2</sub> powder was stirred in ethanol, which acts as a hole scavenger, in a sealed vial that was purged with nitrogen to eliminate the presence of oxygen containing species that would scavenge excited electrons. After irradiation, the white suspension turned dark blue, indicating the presence of excited electrons, in accordance with published results. While electrons are capable of lasting excitation from the valence to conduction band in anatase TiO<sub>2</sub> while holes are scavenged and oxygen is removed from the atmosphere, the photocatalytic activity of anatase TiO<sub>2</sub> in an aqueous medium with exposure to air is poor. P25 nanoparticles were capable of oxidizing dye under the same conditions that anatase TiO<sub>2</sub> failed to oxidize dye: an aqueous medium with exposure to air. Therefore, it can be reasoned that the major contributor to poor photocatalytic activity in anatase TiO<sub>2</sub> is electron – hole combination, because both samples were exposed to oxygen which has the ability to react with excited electrons.

Synthesized TiO<sub>2</sub> – SWNT showed similar performance to anatase TiO<sub>2</sub> and it is currently unclear what is responsible for the lack of photocatalytic activity. TiO<sub>2</sub> – GO samples synthesized following a similar procedure demonstrated electron excitation and transfer from TiO<sub>2</sub> nanoparticles to GO flakes in accordance with published results and as shown in Figure 22. TiO<sub>2</sub> – GO suspended in water and exposed to air changed color, from the brown to black, after

prolonged UV exposure. This indicates the transfer of electrons from  $\text{TiO}_2$  to GO, and the reduction of GO to RGO.<sup>55</sup> It is expected that CNTs, which are analogous in chemical structure to GO, would behave similarly. One explanation for lack of photocatalytic activity of synthesized  $\text{TiO}_2$  – SWNT in comparison to P25 nanoparticles, is that there is less  $\text{TiO}_2$  material in the  $\text{TiO}_2$  – SWNT than in the P25 sample. Each sample tested had a similar mass, however, P25 nanoparticles are 100%  $\text{TiO}_2$ . The percentage of the total  $\text{TiO}_2$  – SWNT mass coming from  $\text{TiO}_2$  is not known, however there is less  $\text{TiO}_2$  in this sample than in the P25 sample. There is also less  $\text{TiO}_2$  in the  $\text{TiO}_2$  – SWNT sample than in the anatase  $\text{TiO}_2$  sample, even though both samples show similar performance. This may indicate the presence of oxidized SWNTs improves photocatalytic activity in comparison to pure anatase  $\text{TiO}_2$  but still does not compare to the ability of P25 to oxidize dye. Another possible reason for the poor photocatalytic activity of  $\text{TiO}_2$  may be a result of the lack of crystalline structure. It is known crystalline structure effects band gap and photocatalytic activity. The current amorphous structure may be unfavorable for photo-oxidation of organic dyes.

Exposure to UV light has been shown to reduce GO in  $\text{TiO}_2$  – GO heterogeneous photocatalysts within 6 hours. Prolonged exposure to UV in the presence of water has been shown to possibly damage the  $\text{TiO}_2$  – RGO structure, as shown in Figure 23. TEM images show that prior to UV exposure,  $\text{TiO}_2$  – GO has the appearance of smooth flakes of graphene with spherical nanoparticles attached at the edges. After 30 hrs of UV exposure, the flakes appear jagged and broken and no spherical particles are found at the edges of the flakes. It's possible that while electrons generated in the  $\text{TiO}_2$  nanoparticles are being “consumed” by the GO flake, water is being oxidized to form ROS which may oxidized the graphene flake. Further studies need to be done to conclude whether or not ROS are being formed and if the graphene lattice is

being oxidized. Simple chemical tests exist to determine ROS concentrations, and Raman spectroscopy could prove useful in determining the quantity of defects before and after UV exposure.

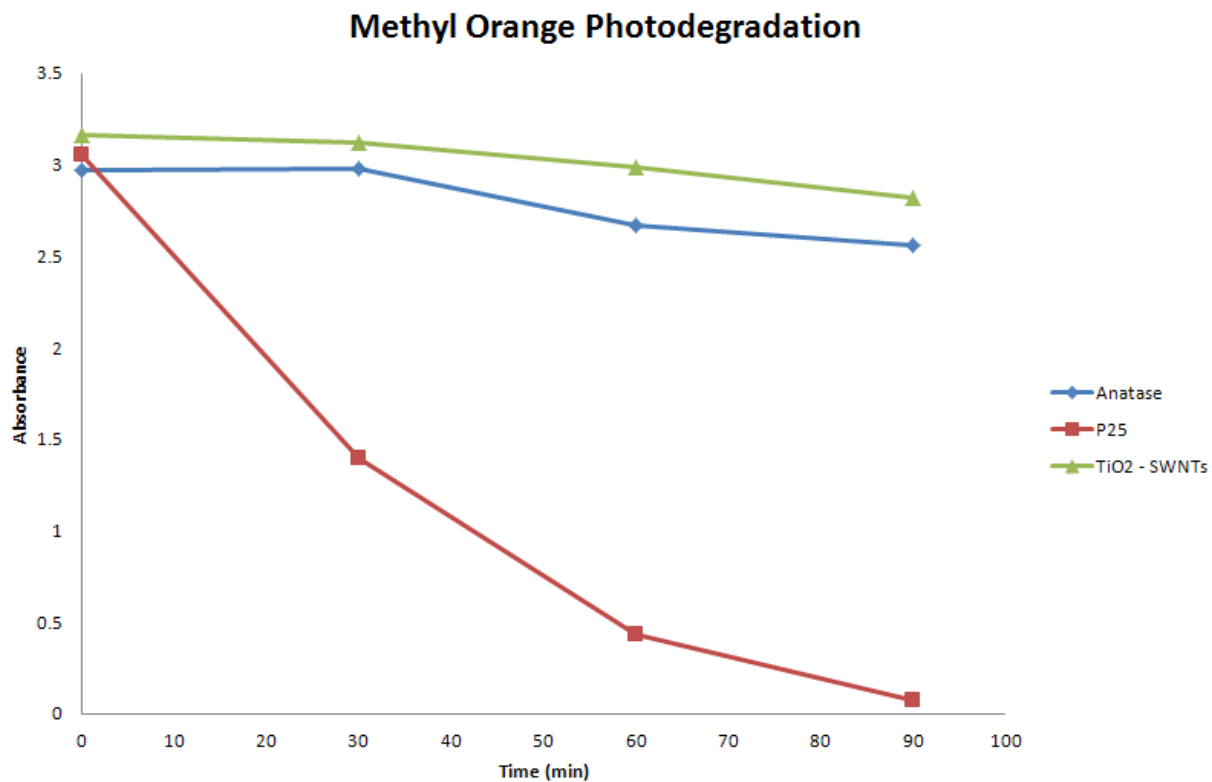
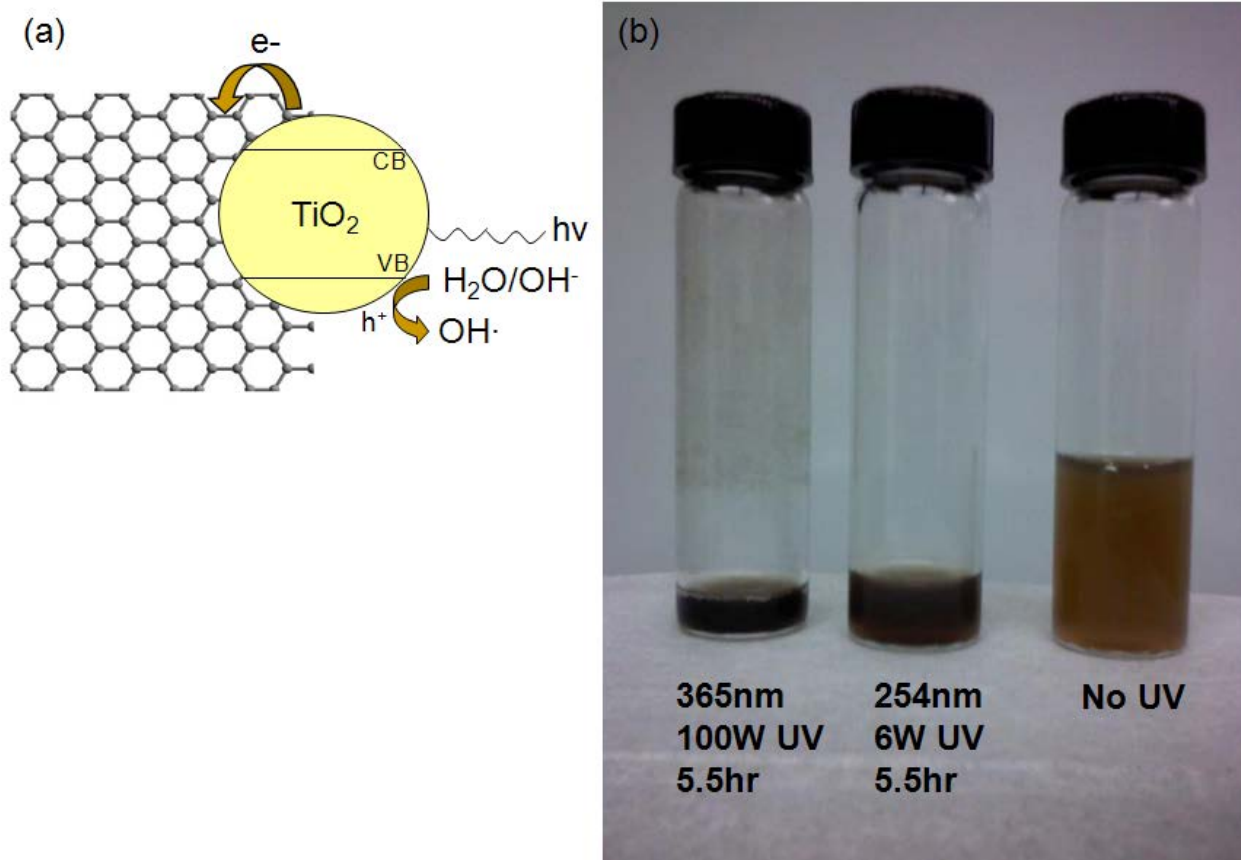
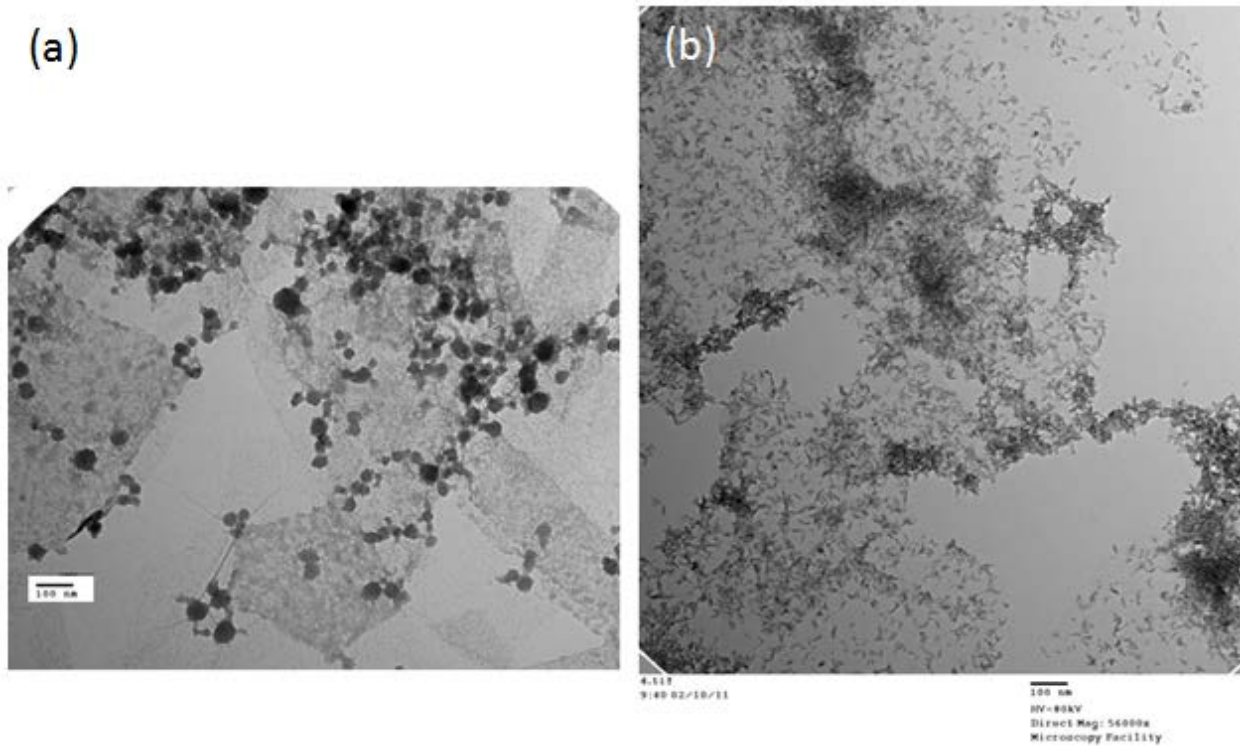


Figure 21 Dye degradation with different photocatalysts



**Figure 22 Photocatalytic electron transfer in  $\text{TiO}_2$  – GO** (a) Illustration of electron transfer in  $\text{TiO}_2$  – GO heterogeneous photocatalysts (b)  $\text{TiO}_2$  – GO before and after UV irradiation



**Figure 23**  $\text{TiO}_2$  – GO before and after UV exposure (a) before UV (b) after 30 hours of UV exposure with 100W, 365nm lamp

### 3.2.3 CO<sub>2</sub> reduction

It was demonstrated that CO<sub>2</sub> can be reduced to hydrocarbons using water and pure TiO<sub>2</sub> as a photocatalyst, albeit in small yields.<sup>31</sup> The reduction of CO<sub>2</sub> to hydrocarbons and small chain alcohols has also been demonstrated for copper doped TiO<sub>2</sub> materials. It has been reported that copper doping of TiO<sub>2</sub> nanoparticles has improved the CO<sub>2</sub> reduction product yield by electron trapping and preventing electron – hole recombination. Suggested mechanisms for CO<sub>2</sub> reduction are shown in Figure 24. It was hypothesized that doping TiO<sub>2</sub> with graphene oxide (GO) or SWNTs may further improve photocatalytic activity of TiO<sub>2</sub> photocatalysts due to the electronic and physical properties of carbon based nanomaterials, as well as their ability to interact with the surface of metal oxides.

There were no indications of the formation of CO<sub>2</sub> reduction products using the TiO<sub>2</sub> – oxidized SWNT photocatalyst sample, as shown in Figure 25. All m/z intensities look similar before and after UV irradiation. This result is not surprising since the same sample showed little photocatalytic efficiency for dye degradation. It is possible that electron – hole recombination or failure to excite electrons is preventing the reduction of CO<sub>2</sub> using TiO<sub>2</sub> – oxidized SWNTs since they showed little efficiency in oxidizing methyl orange, but P25 nanoparticles proved to be capable to eliminating the majority of the color of the dye. Limited SWNT surface area available for CO<sub>2</sub> adsorption may have also prevented CO<sub>2</sub> reduction.<sup>49</sup> SWNTs act as an “electron sink” in a similar fashion to the way metals interact with TiO<sub>2</sub>. Therefore, reduction of a substrate must occur on the surface of the SWNT. If the SWNTs are mostly covered by TiO<sub>2</sub> in a core – shell structure, there is little SWNT surface area available for electron transfer from the SWNT to CO<sub>2</sub> to take place. Failure to reduce CO<sub>2</sub> may have been a result of lack of adsorption of CO<sub>2</sub> on the surface of the carbon nanomaterial support or inability to transfer

electrons from the supporting material to the adsorbed molecules. If it was shown that electrons transfer from TiO<sub>2</sub> to an oxidized carbon substrate such as GO and reduce it, then possibly the electrons are reducing functional groups in the SWNTs and not being transferred from the SWNT surface to CO<sub>2</sub> molecules. Raman and UV-VIS-NIR spectroscopy could prove useful in determining changes to the sp<sup>2</sup> lattice before and after UV irradiation. The ability of P25 to reduce CO<sub>2</sub> given these exact conditions should also be investigated. These data should help elucidate the factors limiting CO<sub>2</sub> reduction product yields with synthesized photocatalysts.

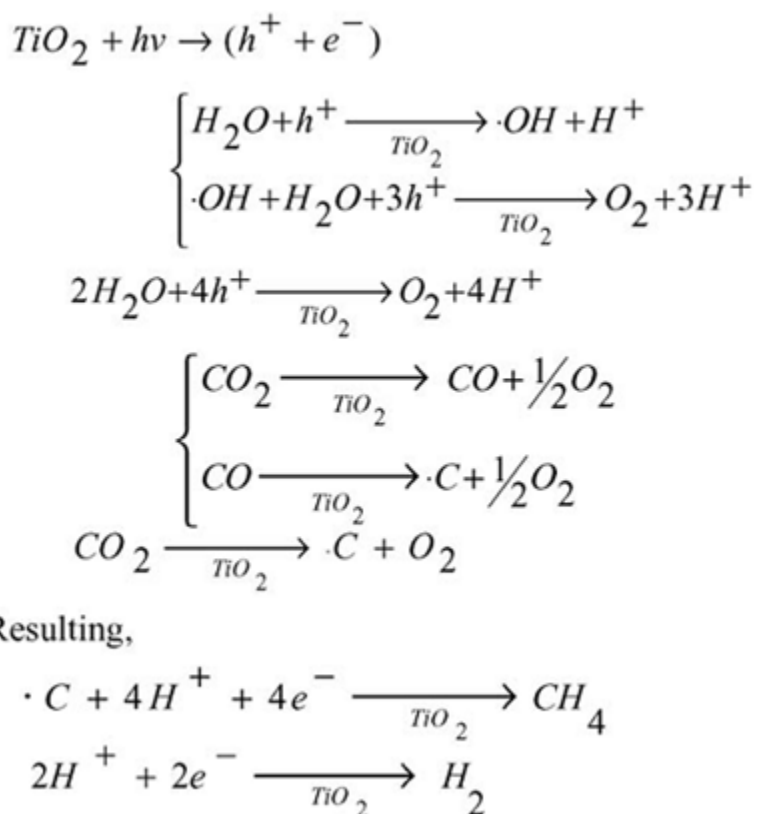
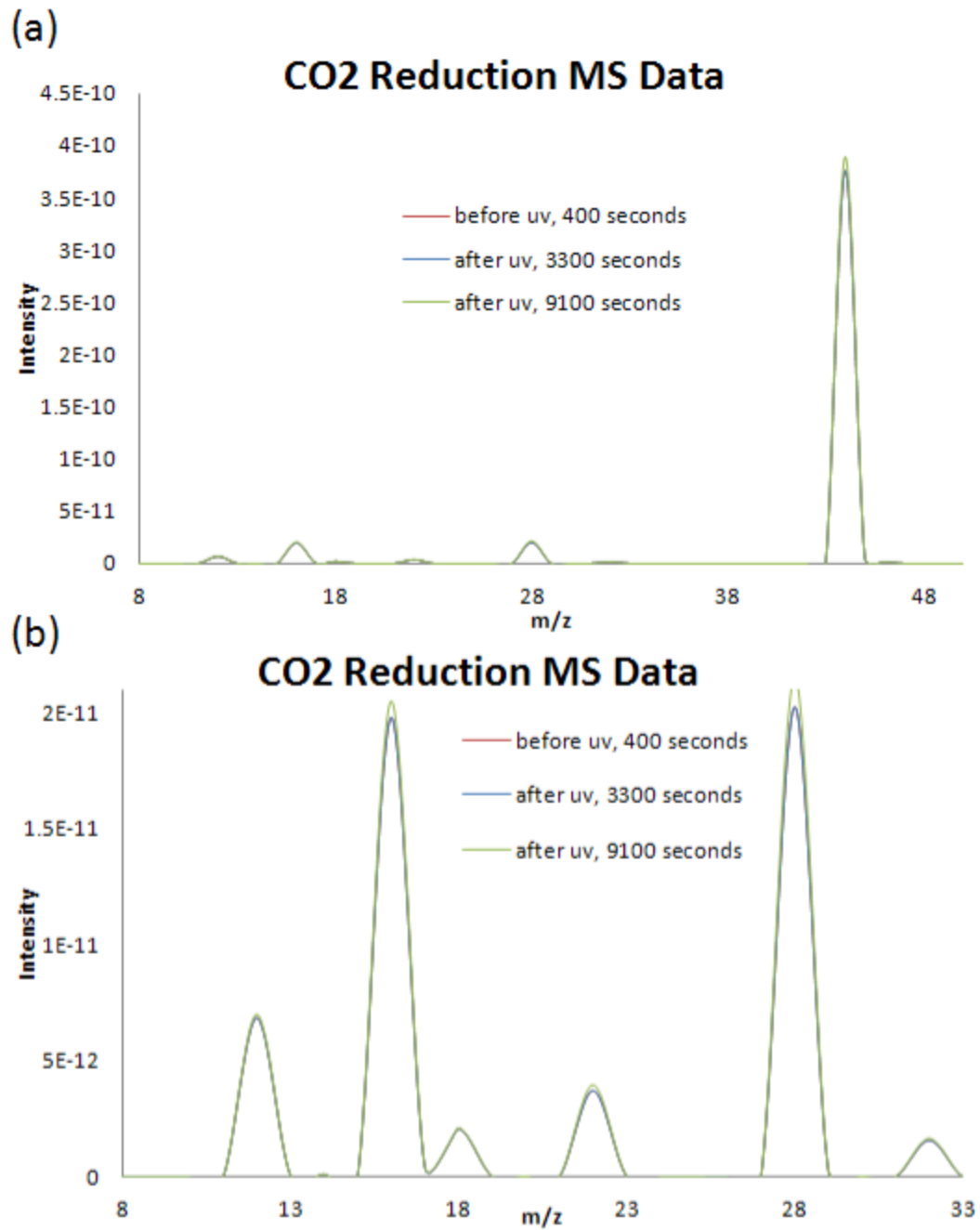


Figure 24 CO<sub>2</sub> reduction mechanisms adapted from reference 30



**Figure 25 CO<sub>2</sub> reduction MS data** (a) MS reduction data (b) close up view of m/z values 8 – 33 from spectra shown in (a)

## APPENDIX A

### TEM IMAGES

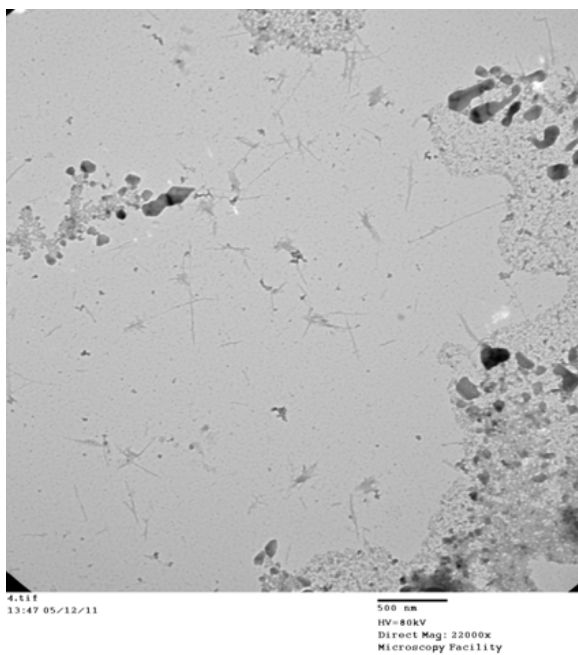


**Figure 26 HRP (1.54 mg) + H<sub>2</sub>O<sub>2</sub> treated H<sub>2</sub>SO<sub>4</sub> / HNO<sub>3</sub> oxidized HiPco SWNTs day 14**

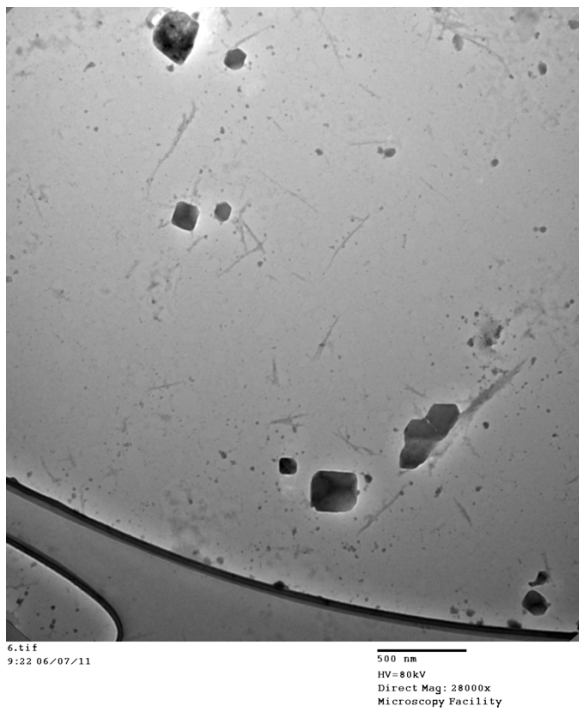


**Figure 27 (1.54 mg) + H<sub>2</sub>O<sub>2</sub> treated H<sub>2</sub>SO<sub>4</sub> / HNO<sub>3</sub> oxidized HiPco SWNTs day 28**

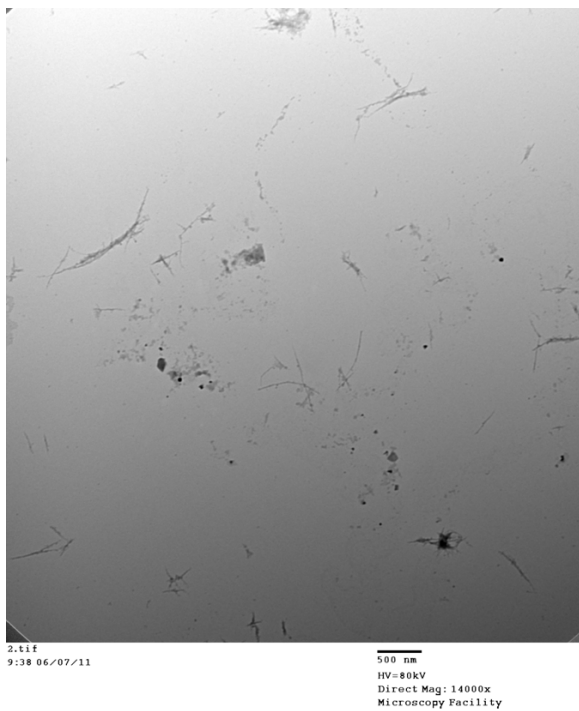


**Figure 28 HRP (0.1 mg) + H<sub>2</sub>O<sub>2</sub> treated H<sub>2</sub>SO<sub>4</sub> / HNO<sub>3</sub> oxidized HiPco SWNTs day 14**

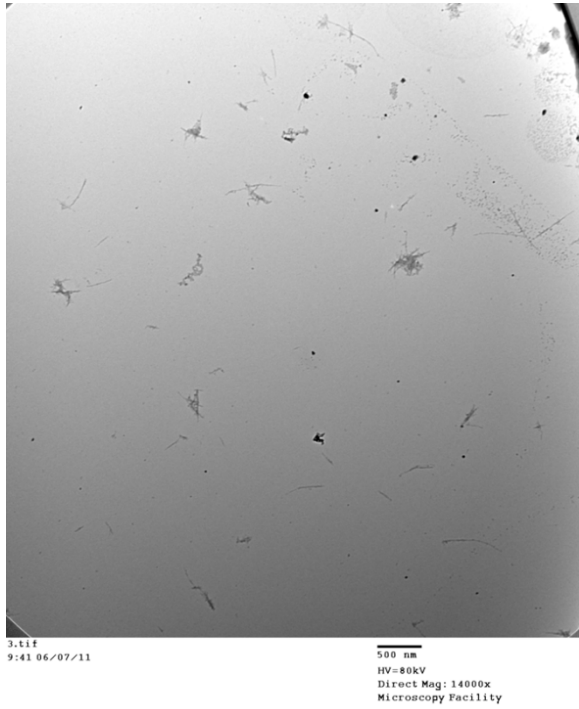


**Figure 29 HRP (0.1 mg) + H<sub>2</sub>O<sub>2</sub> treated H<sub>2</sub>SO<sub>4</sub> / HNO<sub>3</sub> oxidized HiPco SWNTs day 28**

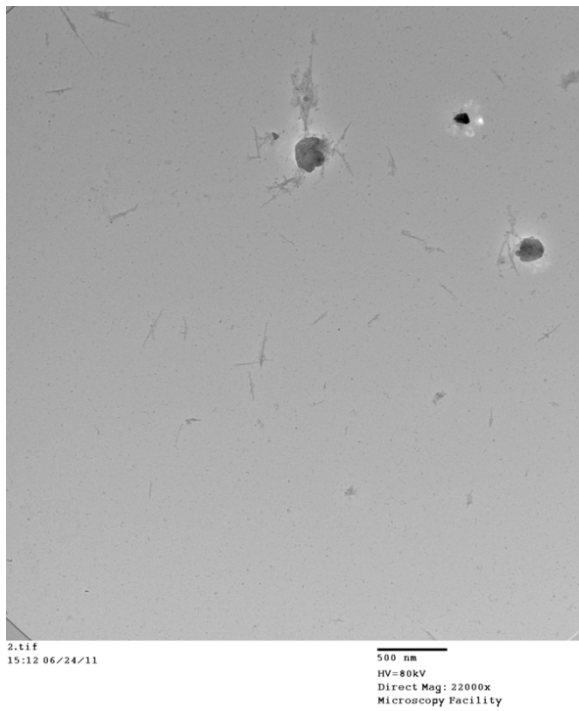


**Figure 30 HRP (0.1 mg) + H<sub>2</sub>O<sub>2</sub> treated H<sub>2</sub>SO<sub>4</sub> / HNO<sub>3</sub> oxidized HiPco SWNTs day 35**

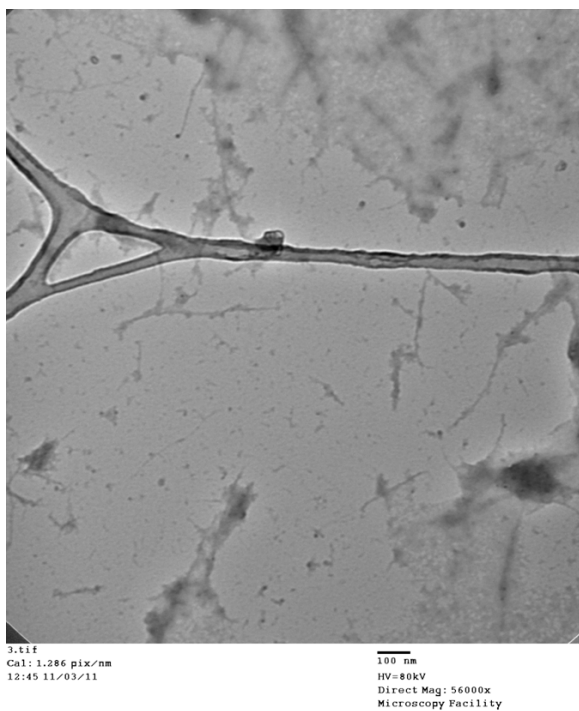


**Figure 31 H<sub>2</sub>O<sub>2</sub> treated (- HRP) H<sub>2</sub>SO<sub>4</sub> / HNO<sub>3</sub> oxidized HiPco SWNTs day 14**

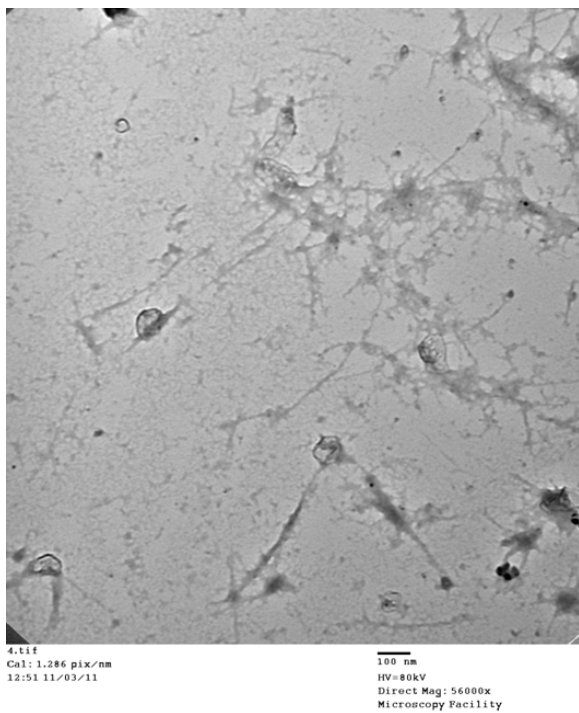


**Figure 32 H<sub>2</sub>O<sub>2</sub> treated (- HRP) H<sub>2</sub>SO<sub>4</sub> / HNO<sub>3</sub> oxidized HiPco SWNTs day 21**

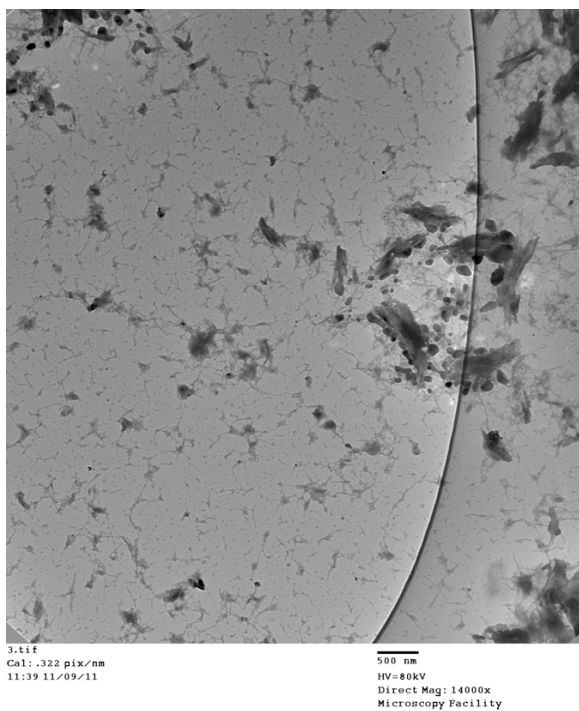


**Figure 33 H<sub>2</sub>O<sub>2</sub> treated (- HRP) H<sub>2</sub>SO<sub>4</sub> / HNO<sub>3</sub> oxidized HiPco SWNTs day 28**

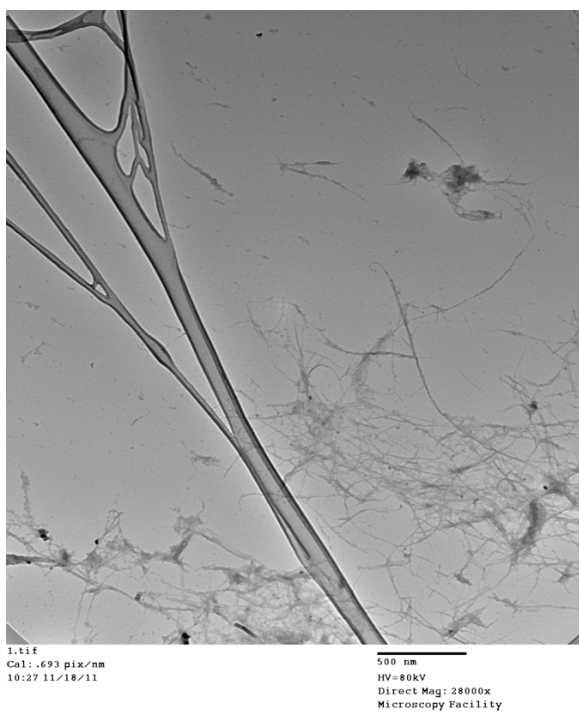


**Figure 34 H<sub>2</sub>O<sub>2</sub> treated (- HRP) H<sub>2</sub>SO<sub>4</sub> / HNO<sub>3</sub> oxidized HiPco SWNTs day 35**

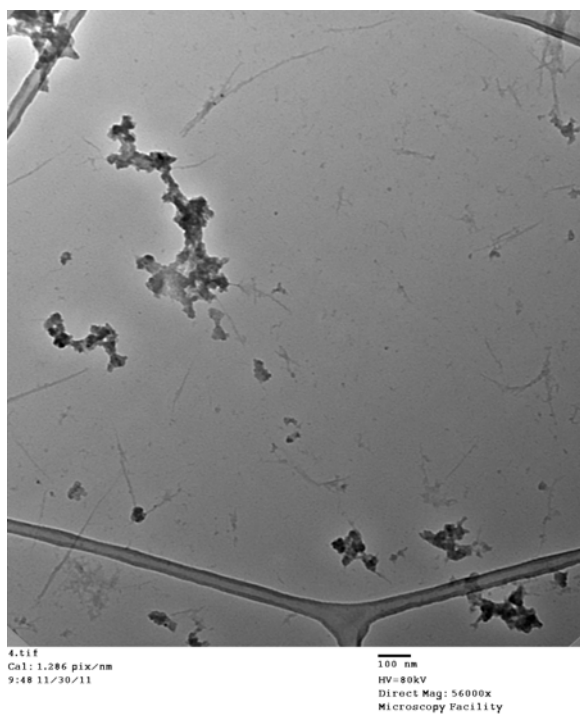


**Figure 35 H<sub>2</sub>O<sub>2</sub> treated (- HRP) H<sub>2</sub>SO<sub>4</sub> / HNO<sub>3</sub> oxidized HiPco SWNTs day 42**

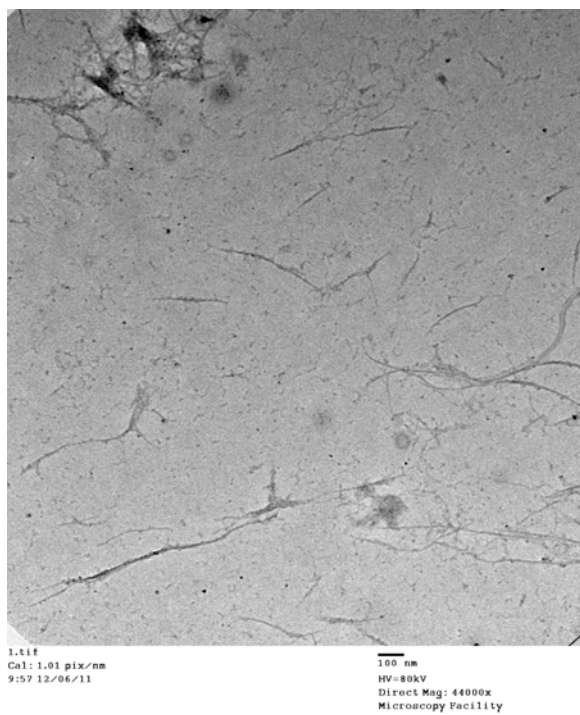


**Figure 36 H<sub>2</sub>O<sub>2</sub> treated (- HRP) H<sub>2</sub>SO<sub>4</sub> / HNO<sub>3</sub> oxidized HiPco SWNTs day 49**

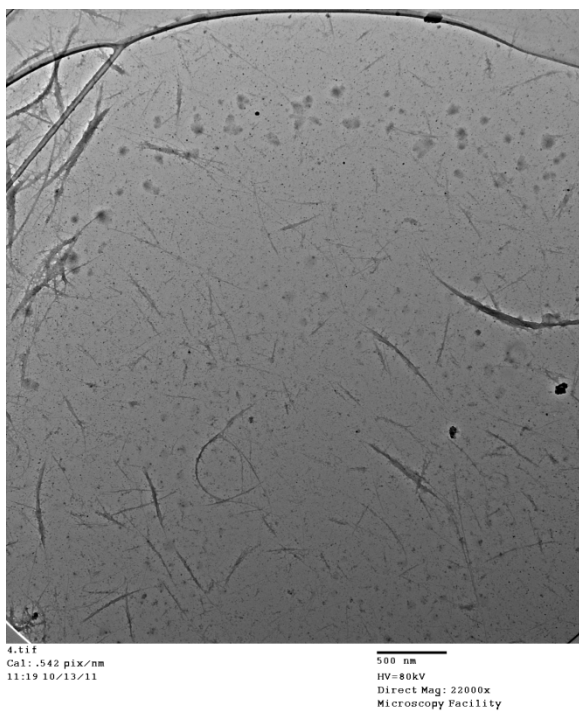


**Figure 37 HRP (1.54 mg) + H<sub>2</sub>O<sub>2</sub> treated H<sub>2</sub>SO<sub>4</sub> / H<sub>2</sub>O<sub>2</sub> oxidized HiPco SWNTs day 7**

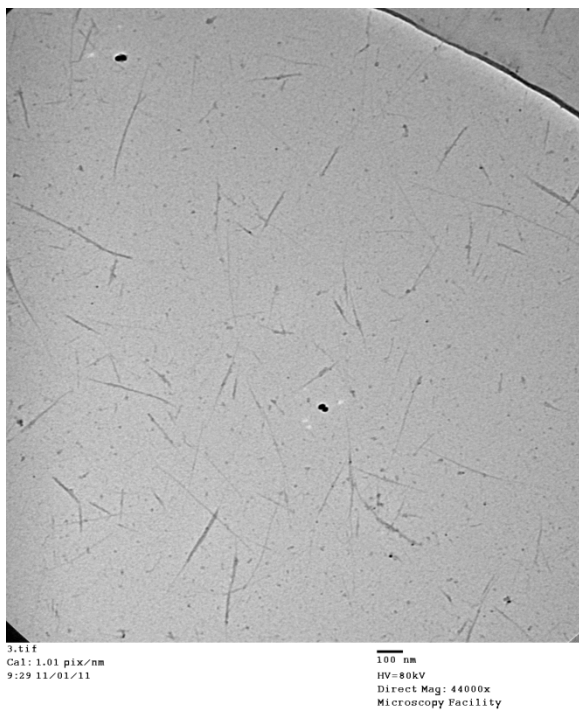


**Figure 38 HRP (1.54 mg) + H<sub>2</sub>O<sub>2</sub> treated H<sub>2</sub>SO<sub>4</sub> / H<sub>2</sub>O<sub>2</sub> oxidized HiPco SWNTs day 14**

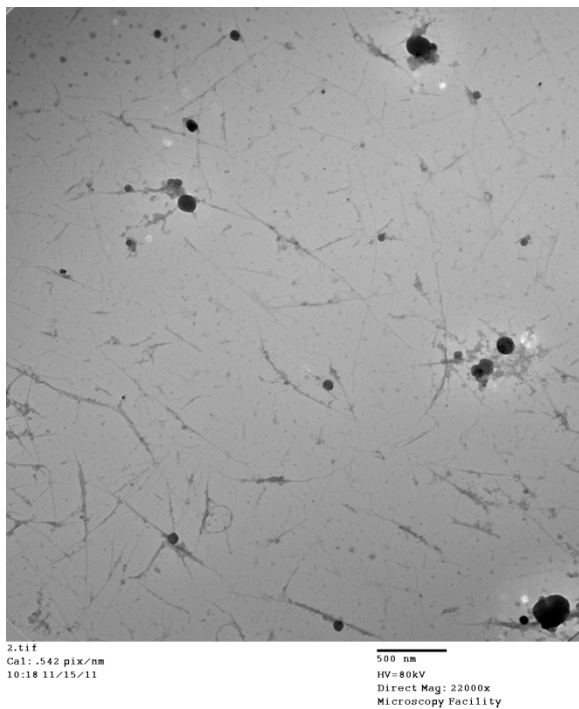


**Figure 39 HRP (1.54 mg) + H<sub>2</sub>O<sub>2</sub> treated H<sub>2</sub>SO<sub>4</sub> / H<sub>2</sub>O<sub>2</sub> oxidized HiPco SWNTs day 21**

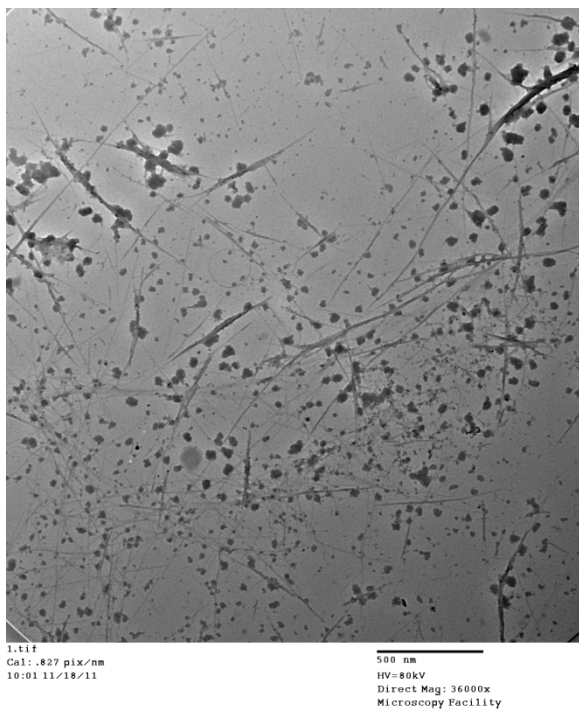


**Figure 40 HRP (1.54 mg) + H<sub>2</sub>O<sub>2</sub> treated H<sub>2</sub>SO<sub>4</sub> / H<sub>2</sub>O<sub>2</sub> oxidized HiPco SWNTs day 28**

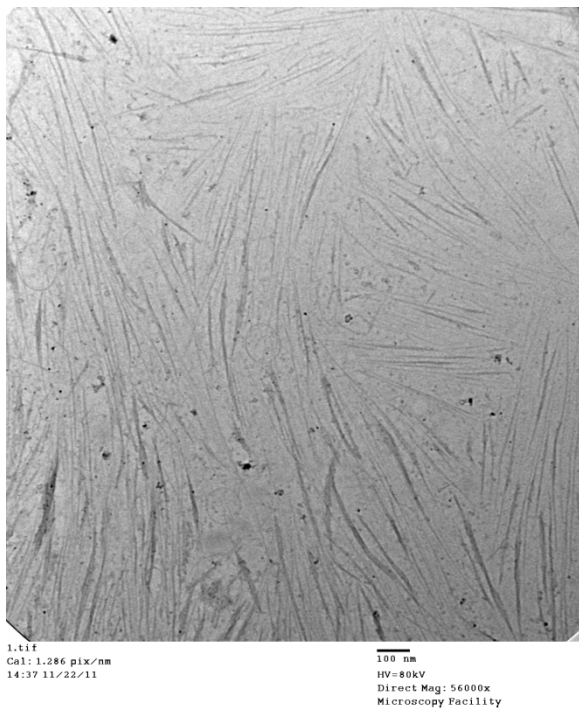


**Figure 41 HRP (1.54 mg) + H<sub>2</sub>O<sub>2</sub> treated H<sub>2</sub>SO<sub>4</sub> / H<sub>2</sub>O<sub>2</sub> oxidized HiPco SWNTs day 35**

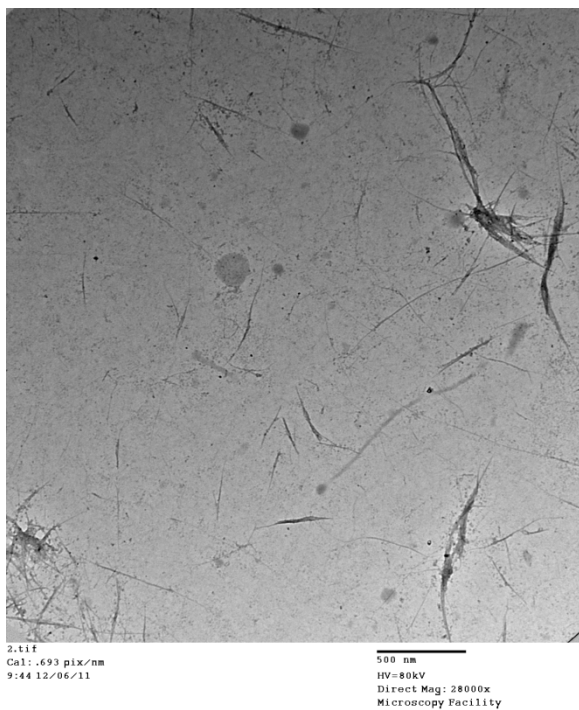


**Figure 42 HRP (1.54 mg) + H<sub>2</sub>O<sub>2</sub> treated H<sub>2</sub>SO<sub>4</sub> / H<sub>2</sub>O<sub>2</sub> oxidized HiPco SWNTs day 42**

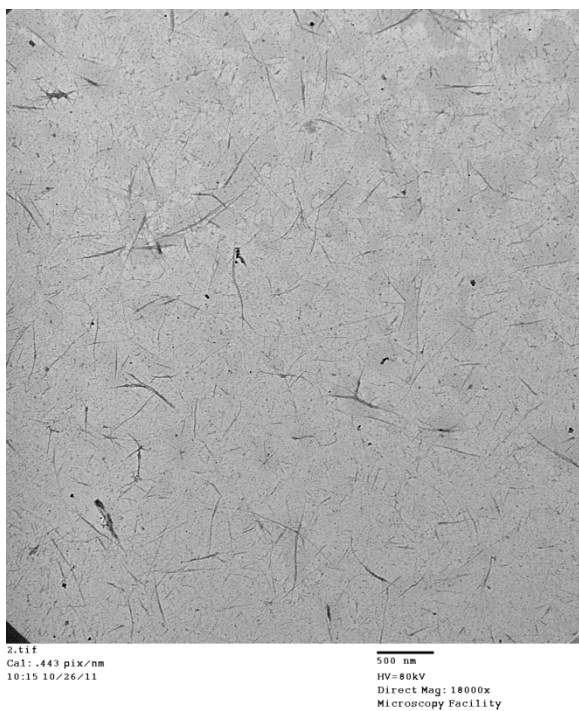


**Figure 43 HRP (0.1 mg) + H<sub>2</sub>O<sub>2</sub> treated H<sub>2</sub>SO<sub>4</sub> / H<sub>2</sub>O<sub>2</sub> oxidized HiPco SWNTs day 7**

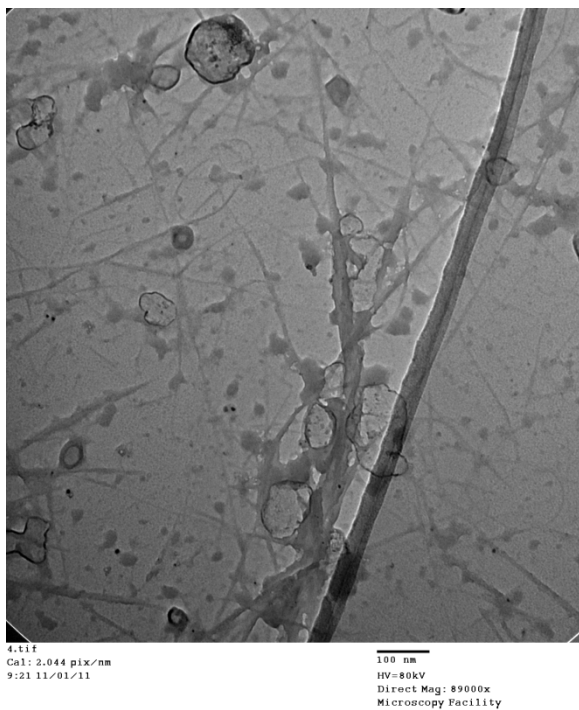


**Figure 44 HRP (0.1 mg) + H<sub>2</sub>O<sub>2</sub> treated H<sub>2</sub>SO<sub>4</sub> / H<sub>2</sub>O<sub>2</sub> oxidized HiPco SWNTs day 14**

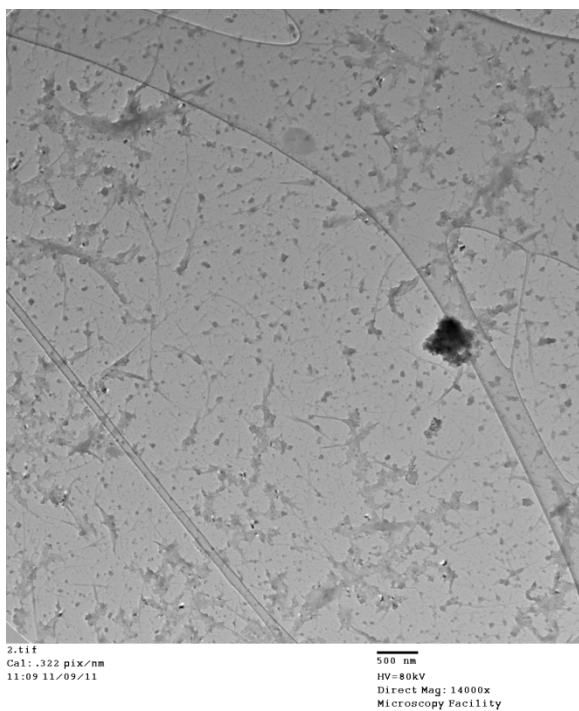


**Figure 45 HRP (0.1 mg) + H<sub>2</sub>O<sub>2</sub> treated H<sub>2</sub>SO<sub>4</sub> / H<sub>2</sub>O<sub>2</sub> oxidized HiPco SWNTs day 21**

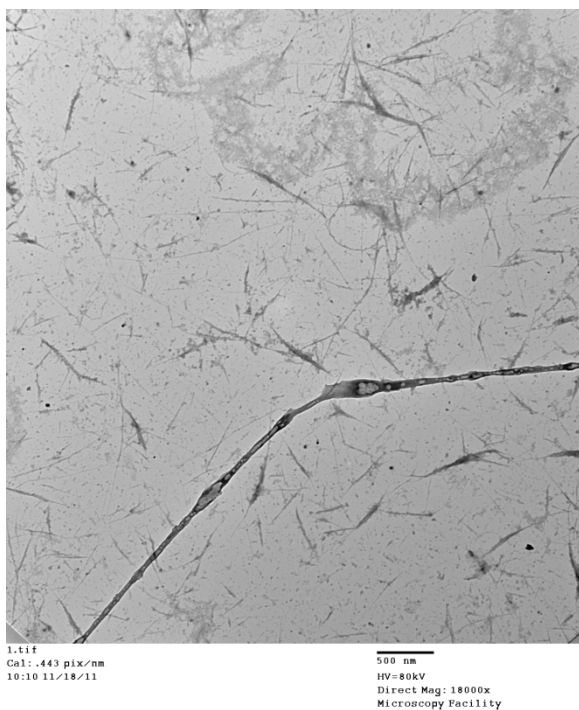


**Figure 46 HRP (0.1 mg) + H<sub>2</sub>O<sub>2</sub> treated H<sub>2</sub>SO<sub>4</sub> / H<sub>2</sub>O<sub>2</sub> oxidized HiPco SWNTs day 28**

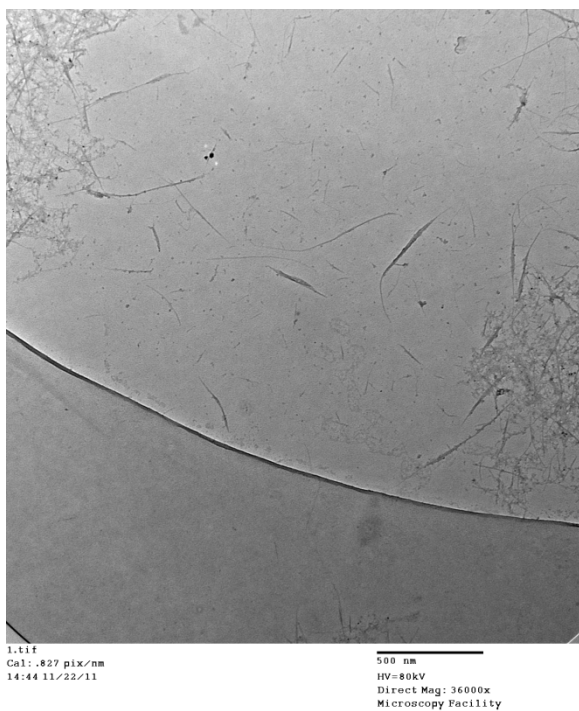


**Figure 47 HRP (0.1 mg) + H<sub>2</sub>O<sub>2</sub> treated H<sub>2</sub>SO<sub>4</sub> / H<sub>2</sub>O<sub>2</sub> oxidized HiPco SWNTs day 35**

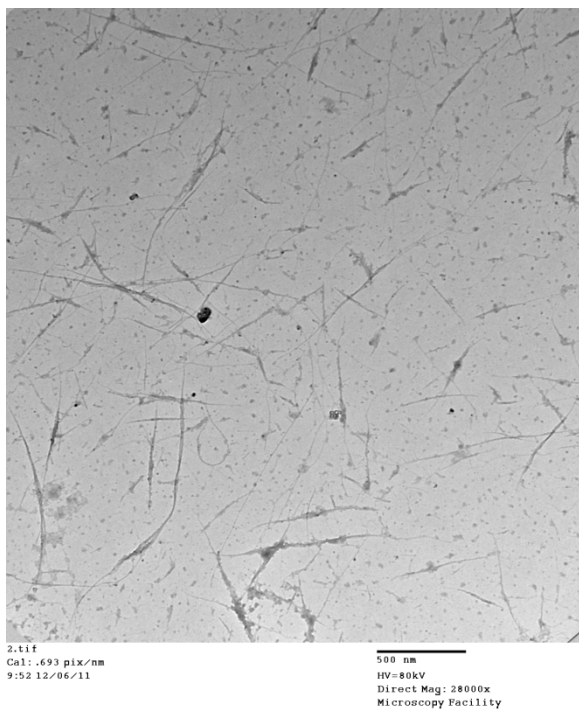


**Figure 48 HRP (0.1 mg) + H<sub>2</sub>O<sub>2</sub> treated H<sub>2</sub>SO<sub>4</sub> / H<sub>2</sub>O<sub>2</sub> oxidized HiPco SWNTs day 42**

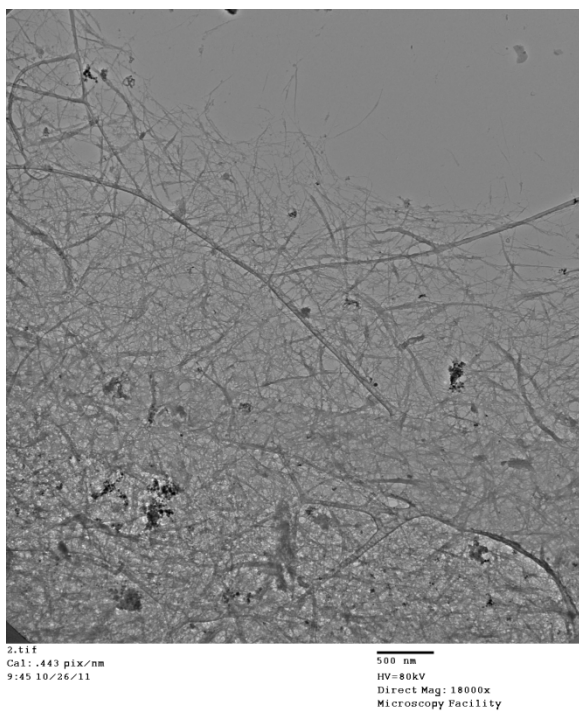


**Figure 49 H<sub>2</sub>O<sub>2</sub> treated (- HRP) H<sub>2</sub>SO<sub>4</sub> / H<sub>2</sub>O<sub>2</sub> oxidized HiPco SWNTs day 7**

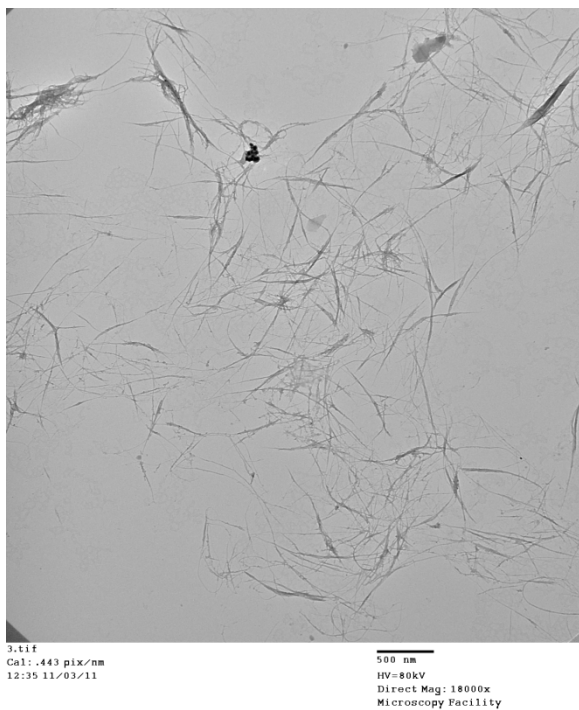


**Figure 50 H<sub>2</sub>O<sub>2</sub> treated (- HRP) H<sub>2</sub>SO<sub>4</sub> / H<sub>2</sub>O<sub>2</sub> oxidized HiPco SWNTs day 14**

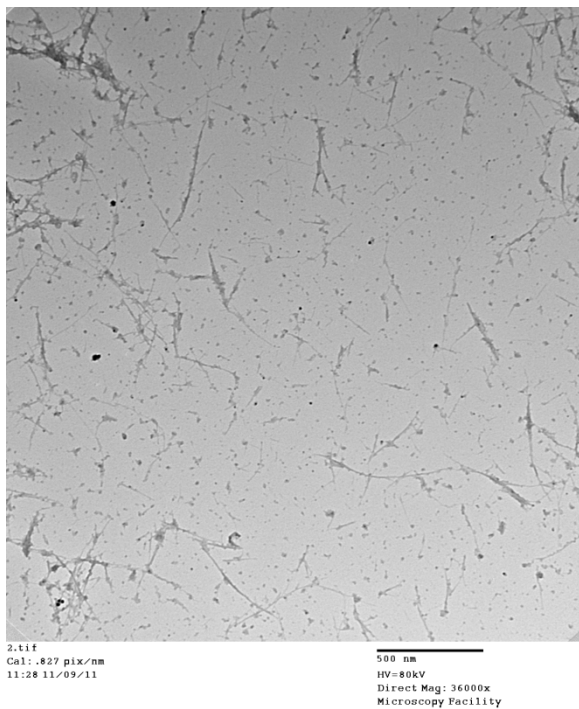


**Figure 51  $\text{H}_2\text{O}_2$  treated (- HRP)  $\text{H}_2\text{SO}_4$  /  $\text{H}_2\text{O}_2$  oxidized HiPco SWNTs day 21**

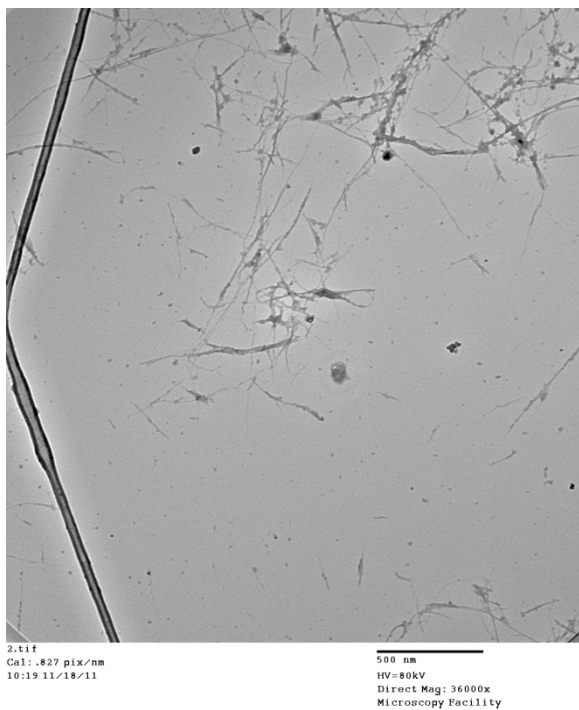


**Figure 52  $\text{H}_2\text{O}_2$  treated (- HRP)  $\text{H}_2\text{SO}_4$  /  $\text{H}_2\text{O}_2$  oxidized HiPco SWNTs day 28**

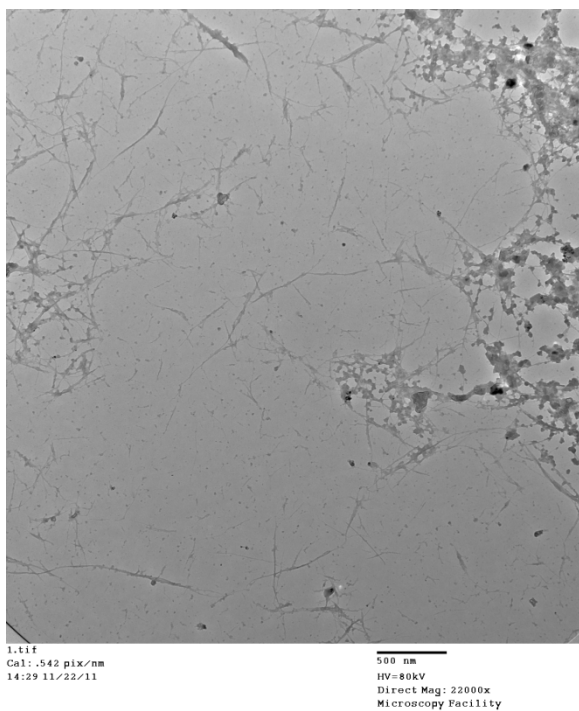


**Figure 53 H<sub>2</sub>O<sub>2</sub> treated (- HRP) H<sub>2</sub>SO<sub>4</sub> / H<sub>2</sub>O<sub>2</sub> oxidized HiPco SWNTs day 35**

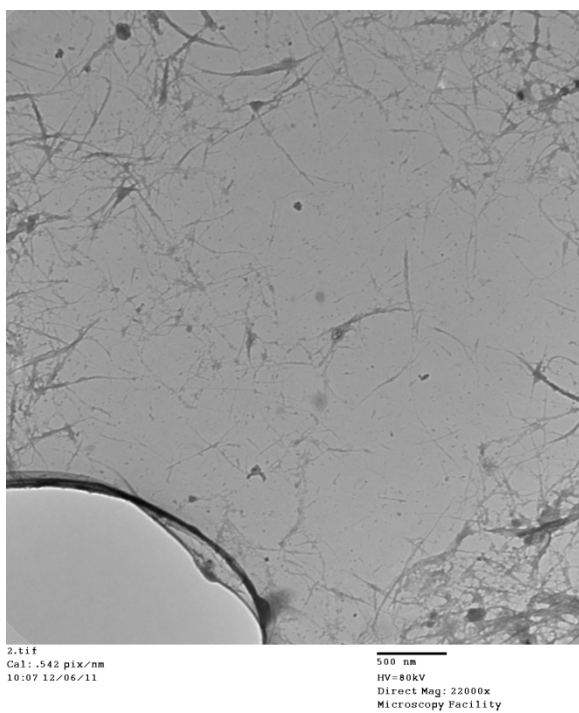


**Figure 54 H<sub>2</sub>O<sub>2</sub> treated (- HRP) H<sub>2</sub>SO<sub>4</sub> / H<sub>2</sub>O<sub>2</sub> oxidized HiPco SWNTs day 42**

## APPENDIX B

### RAMAN SPECTRA

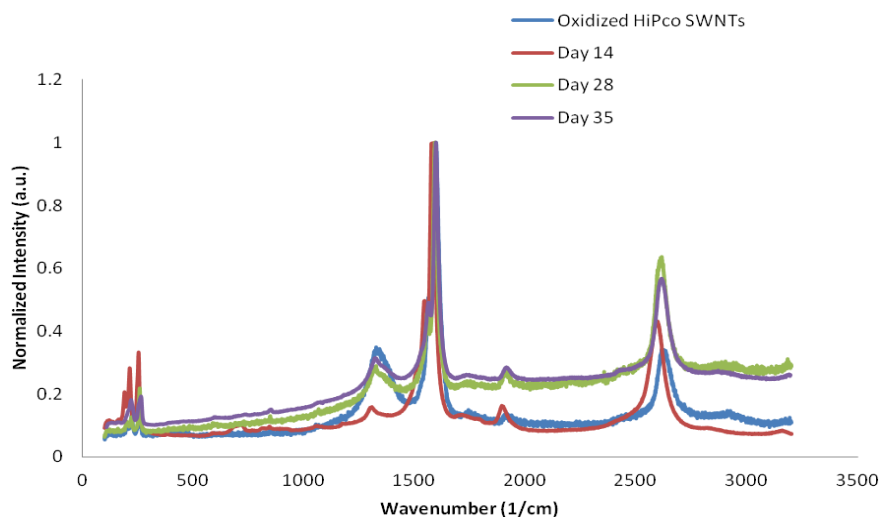


Figure 55 HRP (1.54 mg) + H<sub>2</sub>O<sub>2</sub> treated H<sub>2</sub>SO<sub>4</sub> / HNO<sub>3</sub> oxidized HiPco SWNTs

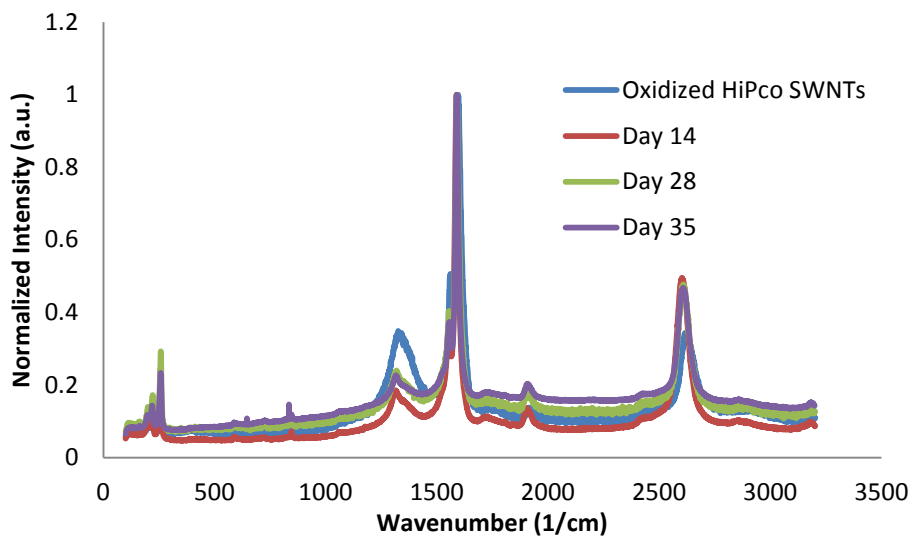


Figure 56 HRP (0.1 mg) + H<sub>2</sub>O<sub>2</sub> treated H<sub>2</sub>SO<sub>4</sub> / HNO<sub>3</sub> oxidized HiPco SWNTs

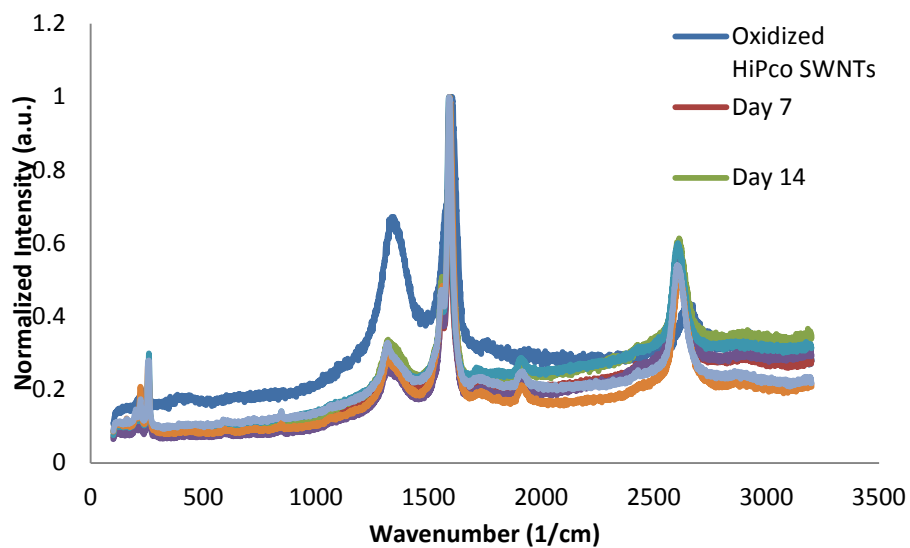


Figure 57 H<sub>2</sub>O<sub>2</sub> treated (- HRP) H<sub>2</sub>SO<sub>4</sub> / HNO<sub>3</sub> oxidized HiPco SWNTs

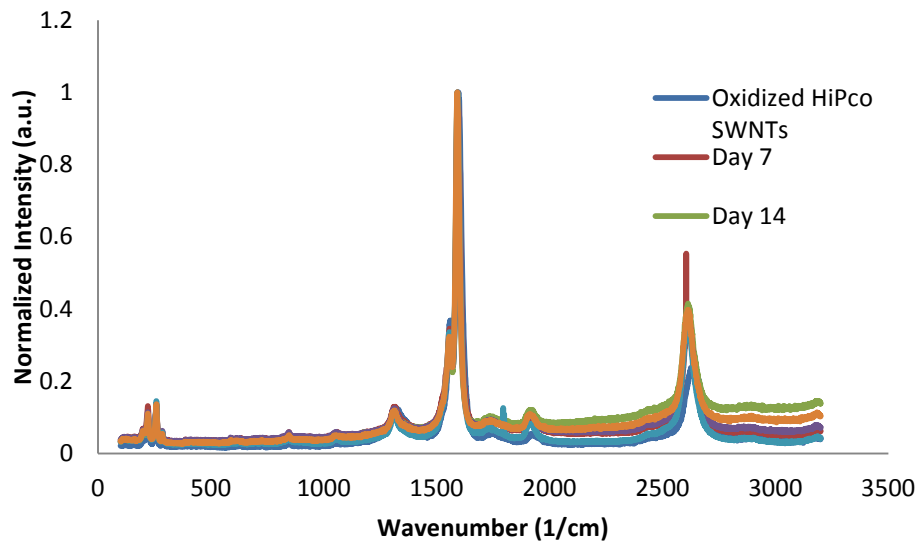


Figure 58 HRP (1.54 mg) + H<sub>2</sub>O<sub>2</sub> treated H<sub>2</sub>SO<sub>4</sub> / H<sub>2</sub>O<sub>2</sub> oxidized HiPco SWNTs

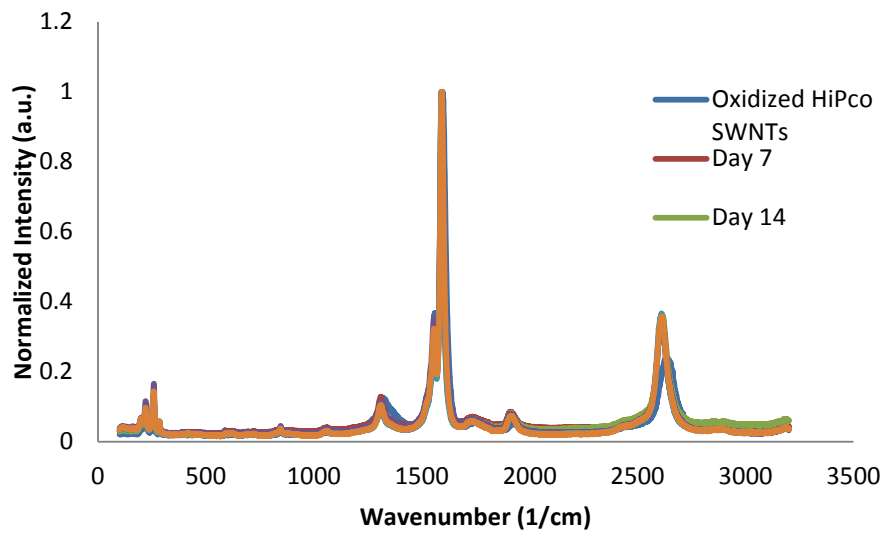


Figure 59 HRP (0.1 mg) + H<sub>2</sub>O<sub>2</sub> treated H<sub>2</sub>SO<sub>4</sub> / H<sub>2</sub>O<sub>2</sub> oxidized HiPco SWNTs

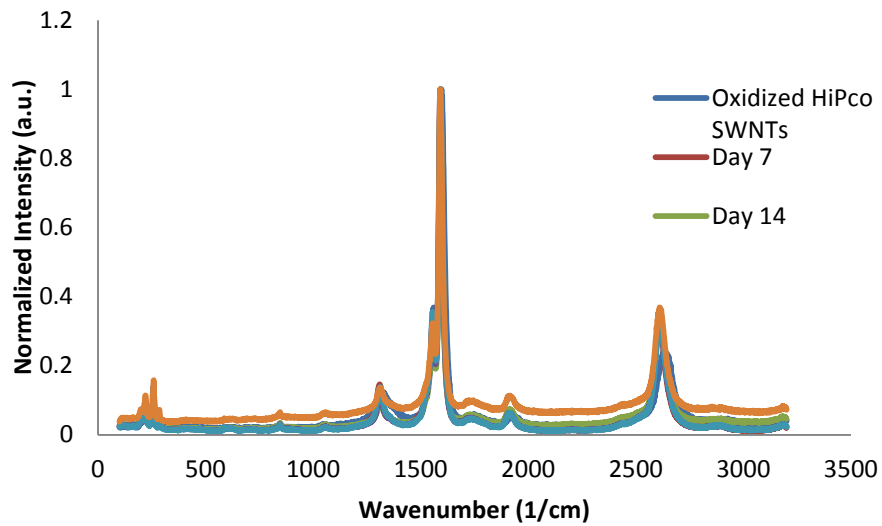


Figure 60 H<sub>2</sub>O<sub>2</sub> treated (- HRP) H<sub>2</sub>SO<sub>4</sub> / H<sub>2</sub>O<sub>2</sub> oxidized HiPco SWNTs

## BIBLIOGRAPHY

- (1) Harper, T., Global Funding for Nanotechnologies & Its Impact July 2011.
- (2) Cao, Q.; Rogers, J. A. *Advanced Materials* **2009**, *21*, 29.
- (3) Ma, X.-w.; Zhao, Y.-l.; Liang, X.-j. *Acta Pharmacol Sin* **2011**, *32*, 543.
- (4) McCarthy, N. *Nat Rev Cancer* **2011**, *11*, 537.
- (5) Schwierz, F. *Nature* **2011**, *472*, 41.
- (6) Odom, T. W.; Huang, J.-L.; Kim, P.; Lieber, C. M. *The Journal of Physical Chemistry B* **2000**, *104*, 2794.
- (7) Balasubramanian, K.; Burghard, M. *Small* **2005**, *1*, 180.
- (8) Iijima, S. *Nature* **1991**, *354*, 56.
- (9) Park, S.; Ruoff, R. S. *Nat Nano* **2009**, *4*, 217.
- (10) Dresselhaus, M. S.; Dresselhaus, G.; Saito, R.; Jorio, A. *Physics Reports* **2005**, *409*, 47.
- (11) Hamada, N.; Sawada, S.-i.; Oshiyama, A. *Physical Review Letters* **1992**, *68*, 1579.
- (12) Saito, R.; Fujita, M.; Dresselhaus, G.; Dresselhaus, M. S. *Electronic structure of chiral graphene tubules*; AIP, 1992; Vol. 60.
- (13) Anantram, M. P.; Léonard, F. *Reports on Progress in Physics* **2006**, *69*, 507.
- (14) Odom, T. W.; Huang, J.-L.; Kim, P.; Lieber, C. M. *Nature* **1998**, *391*, 62.
- (15) Cambridge, U. o. 2007.
- (16) Paredes, J. I. B., M. *Langmuir* **2004**, *20*, 5149
- (17) Robel, I.; Bunker, B. A.; Kamat, P. V. *Advanced Materials* **2005**, *17*, 2458.
- (18) Kongkanand, A.; Kamat, P. V. *ACS Nano* **2007**, *1*, 13.
- (19) Lucchese, M. M.; Stavale, F.; Ferreira, E. H. M.; Vilani, C.; Moutinho, M. V. O.; Capaz, R. B.; Achete, C. A.; Jorio, A. *Carbon* **2010**, *48*, 1592.
- (20) Dresselhaus, M. S.; Jorio, A.; Hofmann, M.; Dresselhaus, G.; Saito, R. *Nano Letters* **2010**, *10*, 751.
- (21) Abdelbary M. A. Elhissi, W. A., Israr Ul Hassan, Vinod. R. Dhanak, and Antony D'Emanuele *Journal of Drug Delivery* **2012**, 2012.
- (22) Chiu-wing, L.; James, J. T.; McCluskey, R.; Arepalli, S.; Hunter, R. L. *Critical Reviews in Toxicology* **2006**, *36*, 189.
- (23) Veitch, N. C. *Phytochemistry* **2004**, *65*, 249.
- (24) Allen, B. L.; Kichambare, P. D.; Gou, P.; Vlasova, I. I.; Kapralov, A. A.; Konduru, N.; Kagan, V. E.; Star, A. *Nano Letters* **2008**, *8*, 3899.
- (25) Allen, B. L.; Kotchey, G. P.; Chen, Y.; Yanamala, N. V. K.; Klein-Seetharaman, J.; Kagan, V. E.; Star, A. *Journal of the American Chemical Society* **2009**, *131*, 17194.

- (26) Berglund, G. I.; Carlsson, G. H.; Smith, A. T.; Szoke, H.; Henriksen, A.; Hajdu, J. *Nature* **2002**, *417*, 463.
- (27) Hayashi, Y. Y., I. *J Biol Chem* **1979**, *254*, 9101
- (28) Veitch, N. C. S., A. T. *Advances in Inorganic Chemistry* **2001**, 107
- (29) D Reyes-Coronado, G. R.-G., M E Espinosa-Pesqueira, C Cab, R de Coss G Oskam *Nanotechnology* **2008**, *19*.
- (30) Amy L Linsebigler, G. L., John T Yates *Chemical Reviews* **1995**, *95*, 735.
- (31) Tan, S. S.; Zou, L.; Hu, E. *Catalysis Today* **2006**, *115*, 269.
- (32) Kočí, K.; Obalová, L.; Matějová, L.; Plachá, D.; Lacný, Z.; Jirkovský, J.; Šolcová, O. *Applied Catalysis B: Environmental* **2009**, *89*, 494.
- (33) Inoue, T.; Fujishima, A.; Konishi, S.; Honda, K. *Nature* **1979**, *277*, 637.
- (34) Rupesh Khare, S. B. *Journal of Minerals & Materials Characterization & Engineering* **2005**, *4*, 31.
- (35) Avouris, P. G. C. a. P. In *Scientific American* 2000, p 62.
- (36) Fadel, T. R.; Look, M.; Staffier, P. A.; Haller, G. L.; Pfefferle, L. D.; Fahmy, T. M. *Langmuir* **2009**, *26*, 5645.
- (37) Shi, X.; von dem Bussche, A.; Hurt, R. H.; Kane, A. B.; Gao, H. *Nat Nano* **2011**, *6*, 714.
- (38) Zhao, Y.; Allen, B. L.; Star, A. *The Journal of Physical Chemistry A* **2011**, *115*, 9536.
- (39) Kagan, V. E.; Konduru, N. V.; Feng, W.; Allen, B. L.; Conroy, J.; Volkov, Y.; Vlasova, I. I.; Belikova, N. A.; Yanamala, N.; Kapralov, A.; Tyurina, Y. Y.; Shi, J.; Kisin, E. R.; Murray, A. R.; Franks, J.; Stolz, D.; Gou, P.; Klein-Seetharaman, J.; Fadeel, B.; Star, A.; Shvedova, A. A. *Nat Nano* **2010**, *5*, 354.
- (40) Nikolaev, P.; Bronikowski, M. J.; Bradley, R. K.; Rohmund, F.; Colbert, D. T.; Smith, K. A.; Smalley, R. E. *Chemical Physics Letters* **1999**, *313*, 91.
- (41) Chiang, I. W.; Brinson, B. E.; Huang, A. Y.; Willis, P. A.; Bronikowski, M. J.; Margrave, J. L.; Smalley, R. E.; Hauge, R. H. *The Journal of Physical Chemistry B* **2001**, *105*, 8297.
- (42) Muramatsu, H.; Hayashi, T.; Kim, Y. A.; Shimamoto, D.; Kim, Y. J.; Tantrakarn, K.; Endo, M.; Terrones, M.; Dresselhaus, M. S. *Chemical Physics Letters* **2005**, *414*, 444.
- (43) Ziegler, K. J.; Gu, Z.; Peng, H.; Flor, E. L.; Hauge, R. H.; Smalley, R. E. *Journal of the American Chemical Society* **2005**, *127*, 1541.
- (44) S. Hussain<sup>1</sup>, P. J., A. Chouksey<sup>3</sup>, R. Raman<sup>3</sup>, S. S. Islam<sup>1</sup>, T. Islam<sup>2</sup>, P. K. Choudhary<sup>3</sup>, Harsh<sup>3</sup> *Journal of Modern Physics* **2011**, 538
- (45) M. Vesali Naseh, A. A. K., Y. Mortazavi, O. Alizadeh Sahraei, F. Pourfayaz, and S. Mosadegh Sedghi *World Academy of Sciences, Engineering and Technology* **2009**, *49*, 177.
- (46) Zhang, J.; Zou, H.; Qing, Q.; Yang, Y.; Li, Q.; Liu, Z.; Guo, X.; Du, Z. *The Journal of Physical Chemistry B* **2003**, *107*, 3712.
- (47) Datsyuk, V.; Kalyva, M.; Papagelis, K.; Parthenios, J.; Tasis, D.; Siokou, A.; Kallitsis, I.; Galiotis, C. *Carbon* **2008**, *46*, 833.
- (48) Liu, X.; Hurt, R. H.; Kane, A. B. *Carbon* **2010**, *48*, 1961.
- (49) Yao, Y.; Li, G.; Ciston, S.; Lueptow, R. M.; Gray, K. A. *Environmental Science & Technology* **2008**, *42*, 4952.
- (50) Niederberger, M. *Accounts of Chemical Research* **2007**, *40*, 793.

- (51) Meyer, T. J.; Meyer, G. J.; Pfennig, B. W.; Schoonover, J. R.; Timpson, C. J.; Wall, J. F.; Kobusch, C.; Chen, X.; Peek, B. M. *Inorganic Chemistry* **1994**, *33*, 3952.
- (52) G. Bertonia, E. B., J. Verbeecka, M. Mertensc, P. Coolb, E.F. Vansantb, G. Van Tendelooa *Ultramicroscopy* **2006**, *106*, 630
- (53) Baiocchi, C.; Brussino, M. C.; Pramauro, E.; Prevot, A. B.; Palmisano, L.; Marci, G. *International Journal of Mass Spectrometry* **2002**, *214*, 247.
- (54) Hurum, D. C.; Agrios, A. G.; Gray, K. A.; Rajh, T.; Thurnauer, M. C. *The Journal of Physical Chemistry B* **2003**, *107*, 4545.
- (55) Williams, G.; Seger, B.; Kamat, P. V. *ACS Nano* **2008**, *2*, 1487.